Supporting Information

Rational Design of an Iridium−Tungsten Composite with an Iridium-Rich Surface for Acidic Water Oxidation

Jiajian Gao,[1] Xiang Huang,[2] Weizheng Cai,[1] Qilun Wang,[1] Chunmiao Jia,[1] and Bin Liu*[,1]

[1]School of Chemical and Biomedical Engineering, Nanyang Technological University, 62 Nanyang Drive, Singapore 637459, Singapore

[2]Department of Physics, Southern University of Science and Technology, No. 1088 Xueyuan Avenue, Nanshan District, Shenzhen 518055, China

*Correspondence to: liubin@ntu.edu.sg (B. Liu)

Experimental Section

Catalyst preparation

Chemicals: iridium (III) chloride hydrate ($IrCl_3 \cdot xH_2O$, reagent grade), ammonium metatungstate hydrate ($(NH_4)_6H_2W_{12}O_{40} \cdot xH_2O$, > 99.0 %), polyethylene glycol 200 ($H(OCH_2CH_2)_nOH$, MW: 190-210, PEG 200), citric acid ($HOC(COOH)(CH_2COOH)_2$, > 99.5 %), iridium black (200 mesh, ≥ 99 % trace metals basis, marked as Ir-SA) and iridium (IV) oxide (99.9 % trace metals basis, marked as IrO_2-SA) were purchased from Sigma-Aldrich and used directly without further purification. Commercial iridium oxide with surface area of 35 m^2/g (product no. 43396, 99.99 % metals basis) and iridium black (product no. 47150, 99.95 % metals basis) with surface area of 27 m^2/g bought from Alfa Aesar were marked as IrO_2-AA and Ir-AA, respectively. De-ionized water was obtained from Millipore Q water purification system. Tungsten incorporated iridium oxides ($IrWO_x$) with different molar ratios of tungsten to iridium were synthesized via the following sol-gel process: in a typical synthesis, 0.35 g iridium (III) chloride hydrate and 3.0 g ammonium metatungstate hydrate were dissolved in 25 mL of de-ionized water at room temperature in a beaker, followed by adding 20 mL PEG 200 and 50 g citric acid. The obtained mixture was stirred overnight to form a uniform sol. Subsequently, the sol was heated to 80 ^oC in an oil bath under stirring to evaporate water and it took about one week to form a dry gel. Afterwards, the resultant gel was calcined at 600 ^oC for 5 h under flowing air (~ 500 mL/min) to remove organic species in a tube furnace at a ramp rate of 2 ^oC/min. The obtained sample with nominal iridium to tungsten molar ratio of 1 : 10 was marked as $Ir_{0.1}WO_x$. $IrWO_x$ composite with iridium to tungsten molar ratio of 1:5 (marked as $Ir_{0.2}WO_x$) was prepared by the above sol-gel method except that 0.7 g of iridium (III) chloride hydrate and 3.0 g of ammonium metatungstate hydrate were used. Another $IrWO_x$ composite with iridium to tungsten molar ratio of 1: 2 (marked as $Ir_{0.5}WO_x$) was prepared by the above sol-gel method except that 1.4 g of iridium (III) chloride hydrate and 2.4 g ammonium metatungstate hydrate were used. The repeat synthesis of $Ir_{0.5}WO_x$ was conducted with the same method except 0.35 g of iridium (III) chloride hydrate and

0.6 g of ammonium metatungstate hydrate were used. Pure iridium oxide (marked as IrO_2) and tungsten oxide (marked as WO_3) were also prepared by the same method with 1.5 g iridium (III) chloride hydrate and 3.0 g ammonium metatungstate hydrate, respectively. The temperature-programmed reduction of the $IrWO_x$ composites, IrO_2, and WO_3 by hydrogen (5 vol.% H_2 balanced with Argon) were conducted on an automated chemisorption analyzer (ChemBET pulsar, Quantachrome). $Ir_{0.1}WO_x$ was reduced at 800, 900, and 1000 ^oC (ramp rate at 5 ^oC/min and held at the target temperature for 10 min followed by cooling to room temperature in 5 vol.% H_2) and the obtained samples were passivated in water to prevent spontaneous ignition in air and then dried in an oven at 60 ^oC. The thus obtained catalysts were marked as $Ir_{0.1}W$-800R, $Ir_{0.1}W$-900R, and $Ir_{0.1}W$-1000R, respectively. Similarly, $Ir_{0.5}WO_x$ was also reduced at three temperatures and marked as $Ir_{0.5}W$-800R, $Ir_{0.5}W$-900R, and $Ir_{0.5}W$-1000R, respectively. The synthesized IrO_2 was reduced at 500 ^oC and marked as Ir while the WO_3 reduced at 900 ^oC was marked as W-900R.

Characterization

Powder X-ray diffraction (XRD) patterns were collected on a Bruker D2 Phaser using Cu Kα radiation with a LYNXEYE detector at 30 kV and 10 mA. The morphological information was examined with field-emission scanning electron microscopy (FESEM, JEOL JSM-6700F). Transmission electron microscopy (TEM) characterization was conducted on a JEOL 2100F field emission electron microscope with an energy dispersive X-ray spectroscopy (EDX) analyzer (Oxford Instrument). N_2 adsorption-desorption was performed on an Autosorb-6 (Quantachrome) at 77 K. Before analysis, the samples were degassed at 120 ^oC for 8 h. Brunauer-Emmett-Teller (BET) surface area was calculated by the data in the P/P_o range of 0.05–0.2. Temperature-programmed reduction with H_2 (H_2-TPR) was carried out on an automated chemisorption analyzer (ChemBET pulsar, Quantachrome). Prior to the measurement, about 200 mg of the sample was placed in a quartz U-tube; the H_2-TPR was conducted in a gas mixture of 5 vol. % H_2 in Ar at a flow rate of 30 mL/min. The temperature was raised to the target temperature at a ramping rate of 5 °C/min. The amount of

H_2 consumption along with time was recorded with a thermal conductivity detector (TCD) by comparing the thermal conductivity of the gas (H_2/Ar) before and after passing through the sample, which was heated gradually by a furnace. XPS measurements were carried out on a Thermofisher ESCALAB 250Xi photoelectron spectrometer (Thermo Fisher Scientific) using a monochromatic Al Kα X-ray beam (1486.6 eV). The dissolved iridium or tungsten element during electrochemical stability testing was measured by inductively coupled plasma mass spectrometry (ICP-MS, Elan DRC-e).

Electrochemical measurements

The electrochemical performance of various catalysts was evaluated in a three-electrode configuration with platinum plate (1 cm × 2 cm) as the counter electrode and Ag/AgCl electrode with saturated KCl salt bridge as the reference electrode on a rotating disk electrode (RDE) setup (Pine Research Instrumentation, USA) and by a CHI (660E) potentiostat. 0.1 M $HClO_4$ electrolyte was prepared by diluting concentrated perchloric acid ($HClO_4$, 70 %, 99.999 % trace metals basis) with Milli-Q H_2O (15 MΩ). A reversible hydrogen electrode (RHE) was made with two Pt plates as working and counter electrodes to calibrate the Ag/AgCl electrode. All potentials reported herein are referenced to the (RHE) scale following: $E_{vs\ \mathrm{RHE}} = E_{vs\ \mathrm{Ag/AgCl}} + 0.197\mathrm{V} + 0.059\mathrm{V} \times \mathrm{pH}$. The overpotential η is calculated by: $\eta = E_{vs\ \mathrm{RHE}} - 1.23$ V. To prepare the working electrode, the catalyst ink was prepared by ultrasonically mixing 10 mg of the catalyst powder, 0.98 mL of Milli-Q H_2O, 0.98 mL of isopropyl alcohol, and 40 μL of 5 wt. % D520 Nafion dispersion solution. Then, 5 μL of the ink was drop-casted on freshly polished glassy carbon electrode (5 mm diameter, Pine), which gives a catalyst loading amount of 125 $\mu g/cm^2_{geom}$. The RDE was kept a rotation speed of 1600 rpm for all linear sweep voltammetry (LSV) measurements. Before electrochemical data collection, the working electrode was cycled for several times between 0.3 and 1.5~1.8 V vs. RHE at a scan rate of 500 mV s^{-1} to fully oxidize the catalyst surface and achieve a stable performance. Cyclic voltammograms (CVs) were recorded in the potential range of 0.2 − 1.25 V vs. RHE at 50 mV s^{-1} under static condition in N_2 saturated 0.1 M $HClO_4$. LSV curves were recorded at a

scan rate of 5 mV s^{-1} with solution Ohmic drop correction. The electrochemically active surface area (ECSA) of each catalyst was estimated through the pseudocapacitive charge according to the reported method.[1] The pseudocapacitive charge of each catalyst was determined by integrating the CV from 0.3 V to 1.25 V vs. RHE and dividing by the scan rate of 50 mV/s.[1, 2] Subsequently, a ECSA-charge constant of 1681 cm^2/C was used to calculated the ECSA. It should be noted that the ECSA of tungsten-iridium composite may be overestimated since tungsten would also contribute the current at the chosen potential window, although it could not serve as active site for OER at low overpotential. For stability test, 50 μL catalyst ink was drop-casted on FTO glass (2 cm × 0.5 cm, here glassy carbon electrode was not used because it would be corroded after long term operation in acidic OER condition), giving a catalyst loading of 250 $\mu g/cm^2_{geom}$. Electrochemical AC impedance spectroscopy measurements were performed in the frequency range from 50 kHz to 0.5 Hz with an amplitude of 10 mV at various potentials. All measurements were repeated at least two times to ensure reproducibility. Considering the fact that different catalysts have different surface area and iridium content, the reported current densities were either normalized to the geometrical surface area of the glassy carbon electrode ($mA\ cm^{-2}_{geom}$), the BET surface area of the catalyst ($mA\ cm^{-2}_{oxide}$), the ECSA of the catalyst ($mA\ cm^{-2}_{ECSA}$), or the amount of iridium content in the catalyst ($mA\ mg^{-1}_{Ir}$) for fair comparison. To ensure that the observed oxidation current was from oxygen evolution, a rotating Pt ring disk electrode held at the ORR potential of 0.4 V versus RHE was used to detect O_2 gas generated at the catalyst surface by electrochemical reduction to estimate the faraday efficiency.[3]

MEA test

To prepare the membrane electrode assemblies (MEA), commercial 40% Pt/C purchased from Fuel Cell Store was used as the cathode catalyst, the prepared $Ir_{0.5}W$-900R was employed as the anode catalyst. The catalyst ink was brushed on commercial membrane Nafion N117 with 2 cm^2 of the geometric area. The total loading

of Pt was fixed at 0.5 g/cm^2 on the cathode and Ir loading was controlled at 1.0 mg/cm^2 on anode. Titanium bipolar plate were used on both of anode and cathode. A Ti-foam and carbon paper were used as current collectors for anode and cathode, respectively. The CV curves of the single cell were tested using a potentiostat (CHI 760E), while the LSV curves were collected by a Source Meter (KEITHLEY 2420).

DFT calculation method

The first-principles calculations were carried out using generalized gradient approximation (GGA) in the form of revised Perdew-Burke-Ernzerhof (RPBE) for the exchange-correlation potentials,[4-6] the projector augmented wave method,[7] and a plane-wave basis set of 450 eV, as implemented in the Vienna ab initio simulation package (VASP) with consideration of spin-polarization [8, 9]. The IrO_2(110) and WO_3(001) surfaces were simulated using slab models composed of (2×1) and (2×2) supercells with fifteen and nine atomic monolayers, respectively. The vacuum layers were set to ~13 Å. The surface Brillouin-zones were sampled with Gamma centered k-meshes of 4×4×1 for both systems. During optimization, the bottom three atomic monolayers for IrO_2(110) were fixed at their bulk positions while the rest atomic layers and adsorbates were free to move in all directions. For WO_3(001) surface, in order to eliminate the dipole perpendicular to the surface, we transferred half of the oxygen atoms from the top to the bottom layer.[10, 11] All of the atoms in WO_3(001) slab and adsorbates were freely relaxed during optimization. In addition, we applied the Hubbard-U corrections with U = 6.2 eV to the d-electrons of W following the approach proposed by Dudarev et al.[11, 12] The energies of gas-phase H_2 and H_2O were calculated in a box in the length of 20 Å with Gamma point. The convergence criteria for electronic and ionic iterations were set as 10^{-4} eV and 0.02 eV/Å, respectively. Dipole corrections were considered throughout the calculations.

We consider the oxygen evolution reaction (OER) follows the four-electron mechanism[13], which includes intermediates *OH, *O, and *OOH along the pathway (* represents the active site of the catalysts).

$$* + H_2O_{(l)} \rightarrow *OH + H^+_{(sol)} + e^- \quad (1)$$

$$*OH \rightarrow *O + H^{+}_{(sol)} + e^{-} \quad (2)$$

$$*O + H_2O \rightarrow *OOH + H^{+}_{(sol)} + e^{-} \quad (3)$$

$$*OOH \rightarrow * + O_{2(g)} + H^{+}_{(sol)} + e^{-} \quad (4)$$

The free energies of reactant, product, and reaction intermediate are defined as:

$$G = E_{DFT} + E_{ZPE} - TS$$

where E_{DFT} ,E_{ZPE} , and TS represent the electronic energy, zero point energy, and entropy at 298.15 K. The entropies of gas H_2O and H_2 were obtained from the standard thermodynamic database.[14] For t he reaction step containing transfer of proton and electron, the free energy of a pair of proton and electron ($H^+ + e^-$) was calculated as a function of applied potential relative to reversible hydrogen electrode (U *vs* RHE), i.e., $\mu(H^+) + \mu(e^-) = 0.5\mu(H_2) - eU$.[15] The potential determining step (PDS) is defined as the highest free energy step and therefore it is the last step to become downhill in fr ee energy with the increase of potential.

Table S1. BET surface area and total pore volume of the six samples.

Sample	BET surface area (m^2/g)	Total pore volume (cm^3/g)
$Ir_{0.1}WO_x$	6.7	0.091
$Ir_{0.5}WO_x$	9.7	0.064
IrO_2	7.4	0.079
$Ir_{0.1}$W-900R	5.3	0.064
$Ir_{0.5}$W-900R	8.4	0.032
Ir	6.6	0.065

Table S2. Element composition estimated by XPS and EDX.

Sample	Ir:W:O molar ratio on surface determined by XPS*	Ir:W:O molar ratio in bulk determined by SEM-EDX
$Ir_{0.1}WO_x$	0.26 : 1 : 2.93 (3.52)	0.11 : 1 : 3.11
$Ir_{0.5}WO_x$	0.82 : 1: 4.57 (4.64)	0.55 : 1 : 2.69
$Ir_{0.1}$W-900R	0.29 : 1 : 2.78 (3.58)	0.12 : 1 : 0.60
$Ir_{0.5}$W-900R	1.42 : 1 : 3.82 (5.84)	0.47 : 1 : 0.84

*Note: the number in parentheses is the calculated stoichiometric number of oxygen according to IrO_2 (Ir : O = 1:2) and WO_3 (Ir : O = 1:2). The surface oxygen content of hydrogen reduced $Ir_{0.1}$W-900R and $Ir_{0.5}$W-900R is much lower as compared to $Ir_{0.1}WO_x$ and $Ir_{0.5}WO_x$. Considering the fact that all samples could not be dissolved even in hot aqua regia, the bulk composition could not be precisely determined by inductively coupled plasma (ICP), so we used EDX to estimate the bulk composition. The Ir : W molar ratio in the bulk of Ir0.1WOx (0.11 : 1), $Ir_{0.1}$W-900R (0.12 : 1), $Ir_{0.5}WO_x$ (0.55 : 1), and $Ir_{0.5}$W-900R (0.47 : 1) estimated by SEM-EDX generally agree with the molar ratio of the precursor used in the synthesis (0.1 : 1 for $Ir_{0.1}WO_x$ and $Ir_{0.1}$W-900R while 0.5 : 1 for $Ir_{0.5}WO_x$ and $Ir_{0.5}$W-900R). Moreover, the molar ratio of Ir : W at the surface of the four catalysts estimated by XPS is higher than that in the bulk detected by SEM-EDX, suggesting that the obtained catalysts are surface-rich in iridium, especially for the two reduced catalysts: $Ir_{0.1}$W-900R and $Ir_{0.5}$W-900R.

Table S3. ICP-MS measurement of the electrolyte before and after the CV activation test for all catalysts.

Item		Concentration of iridium (μg/L)	Concentration of tungsten (μg/L)	Weight percent of dissolved iridium (wt%)	Weight percent of dissolved tungsten (wt%)
Fresh electrolyte (background)		0.009	-0.058	NA	NA
Electrolyte after CV activation process	$Ir_{0.1}WO_x$	2.01 (0.91)	2.67 (0.43)	2.62	0.37
	$Ir_{0.5}WO_x$	3.88 (1.02)	2.364 (0.55)	1.46	0.45
	IrO_2	4.42 (0.81)	0.003	0.58	NA
	$Ir_{0.1}$W-900R	1.75 (1.10)	2.364 (0.60)	2.10	0.32
	$Ir_{0.5}$W-900R	5.98 (0.97)	2.616 (0.51)	2.19	0.48
	Ir	15.8 (0.83)	-0.073	1.93	NA

Note: The Ir and W redeposited on the counter Pt electrode was dissolved with aqua regia and added to the electrolyte before ICP analysis. The numbers in the brackets are the standard deviations. The total dissolved iridium of $Ir_{0.1}WO_x$ after CV activation is: 2.01 μg/L × 30 mL = 0.060 μg (30 mL is the volume of the electrolyte), which occupies only 2.62 wt.% of the total iridium loaded (25 μg × 9.2 % = 2.3 μg). Similarly, it can be calculated that the dissolved tungsten occupies only 0.3 wt.% of the total tungsten in the $Ir_{0.1}WO_x$ catalyst. The dissolved iridium and tungsten of other catalysts during CV activation process is calculated by the same method.

Table S4. Activity comparison of IrO_x based OER catalysts.

Catalyst	BET surface area m^2/g	Catalyst loading amount	Electrode material*	Electrolyte	Potential at 10 mA/cm^2_{geom}	Tafel slope $mV\ dec^{-1}$	Potential at 1 mA/cm^2_{oxide}	Potential at 100 mA/mg_{Ir}	Ref.
$Ir_{0.5}W$-900R	8.4	50 $\mu g_{Ir}/cm^2$	GCE	0.1 M $HClO_4$	1.53 V	42	1.53 V	1.52 V	This work
Li-IrO_x	27	50 $\mu g/cm^2$	GCE	0.5 M H_2SO_4	1.53 V	39	1.55 V	1.52 V	16
$NiIrO_x$	NA	10 $\mu g_{Ir}/cm^2$	GCE	0.05 M H_2SO_4	NA	NA	NA	1.48 V	17
IrO_2 nanoparticles	71	50 $\mu g/cm^2$	GCE	0.1 M $HClO_4$	1.66 V	45	1.59 V	1.56 V	18
IrO_x	N.A.	N.A.	GCE	1.0 M H_2SO_4	1.57 V	N.A.	N.A.	N.A.	19
Ir nanodendrites	39.2	10.2 μg_{Ir} /cm^2	GCE	0.05 M H_2SO_4	1.63 V	56	1.57 V	1.52 V	20
IrO_2 NP	N.A.	15 $\mu g/cm^2$	Au disk	0.1 M $HClO_4$	N.A.	57	1.59 V	N.A.	21
Ba_2YIrO_6	N.A.	15 $\mu g/cm^2$	Au disk	0.1 M $HClO_4$	N.A.	67	1.56 V	N.A.	21
$Y_2Ir_2O_7$	40	400 $\mu g/cm^2$	GCE	0.1 M $HClO_4$	N.A.	50	N.A.	1.54 V	22
$IrO_x/SrIrO_3$	N.A.	N.A.	$SrIrO_3$	0.5 M H_2SO_4	1.52 V	40	1.47 V	N.A.	23
Ir oxohydroxides	N.A.	100 $\mu g_{Ir}/cm^2$	ATO	0.5 M H_2SO_4	1.54 V	N.A.	N.A.	N.A.	24
IrO_x	150	100 $\mu g/cm^2$	GCE	0.1 M $HClO_4$	N.A.	44	N.A.	1.54 V	25
$IrNiO_x$	N.A.	N.A.	Ti cylinders	0.1 M $HClO_4$	1.54 V	N.A.	N.A.	N.A.	26

*GCE: glassy carbon electrode; ATO: antimony-doped tin oxide.

Table S5. ICP-MS measurement of the electrolyte before and after the stability test of $Ir_{0.5}W$-900R, Ir-AA, and IrO_2-AA.

Item	Concentration of iridium (μg/L)	Concentration of tungsten (μg/L)
Fresh electrolyte (background)	0.0203 (0.00089)	0.062 (0.0027)
Electrolyte after 100 h stability test of $Ir_{0.5}W$-900R	24.4 (0.24)	3.73 (0.17)
Electrolyte after 100 h stability test of Ir-AA	82.3 (0.87)	0.0669 (0.0044)
Electrolyte after 100 h stability test of IrO_2-AA	72.8 (0.71)	0.0554 (0.0036)

Note: The Ir and W redeposited on the counter Pt electrode was dissolved with aqua regia and added to the electrolyte before ICP analysis. The number in the brackets is the standard deviation. The total dissolved iridium of $Ir_{0.5}W$-900R after 100 h stability test at 10 mA/cm^2 is: 24.4 μg/L × 120 mL = 2.93 μg (120 mL is the volume of the electrolyte), which occupies only 3.6 wt. % of the total iridium loaded (250 μg/cm^2 × 1 cm^2 × 33 % = 82.5 μg). Similarly, it can be calculated that the dissolved tungsten occupies only 0.3 wt. % of the total tungsten in the catalyst. In contrast, the dissolution rate of iridium in commercial Ir-AA and IrO_2-AA is about three times higher compared with that of $Ir_{0.5}W$-900R, suggesting tungsten matrix did stabilize iridium during OER process.

Estimation of electrical conductivity of the catalysts

The conductivity of the samples was estimated by the following method: 100 mg of sample powder was compressed into a tablet with diameter of 5 mm and height of ~2 mm at a pressure of 20 MPa in a tableting machine, and then the CV curves of the samples were collected on a CHI760E potentiostat. The reference and counter electrode cables were connected to the top of the cylinder and the working electrode cable was connected to the bottom of the cylinder. The CV scan was conducted in the potential range from -0.05 to 0.05 V at a scan rate of 5 mV/s, while the CV curves of WO_3 and $Ir_{0.1}WO_x$ were collected from -1 V to 1 V at a scan rate of 100 mV/s. It can be estimated that the conductivity of WO_3 and $Ir_{0.1}WO_x$ is relatively lower as compared to other samples (Figure S1b). $Ir_{0.5}WO_x$ shows increased conductivity compared with pure WO_3 and $Ir_{0.1}WO_x$ resulting from the introduction of IrO_2 (Figure S1a). After reduction with hydrogen at 900 °C, the obtained $Ir_{0.1}$W-900R and $Ir_{0.5}$W-900R show much enhanced conductivity compared to the corresponding unreduced oxides.

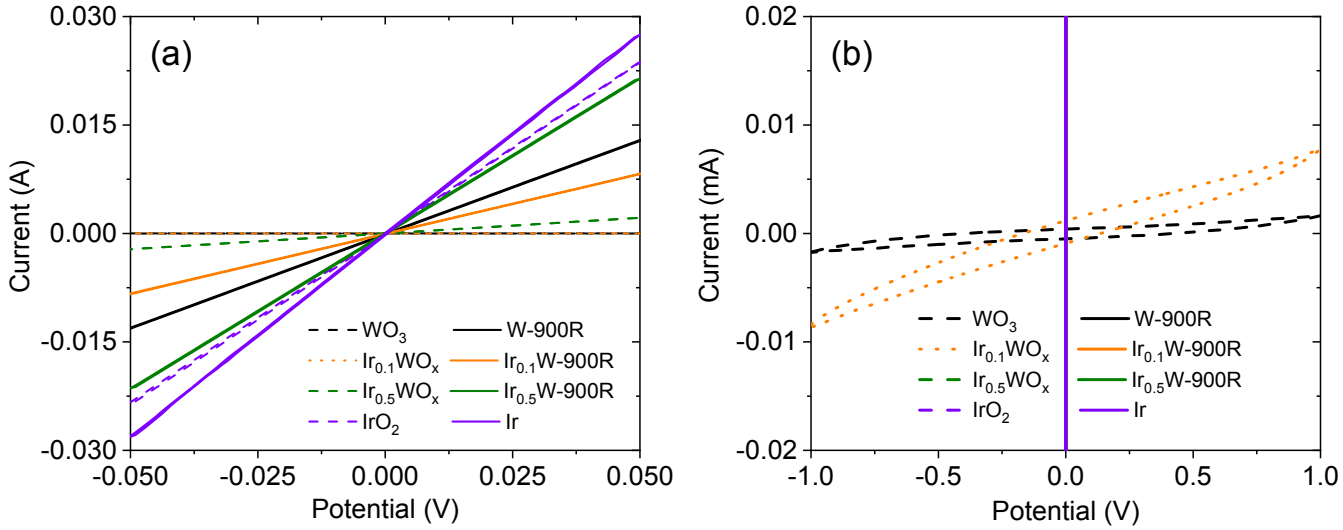

Figure S1. (a) CV curves of pressed samples to estimate the electrical conductivity, and (b) shows an enlarged part of (a). Note: The CV curves of WO_3 and $Ir_{0.1}WO_x$ are overlapped in (a). Different current unit (mA) and potential range (-1 V ~1 V) are used in (b) in comparison with (a). The CV curves of $Ir_{0.5}WO_x$, IrO_2, W-900R, $Ir_{0.1}$W-900R, $Ir_{0.5}$W-900R, and Ir are overlapped in (b).

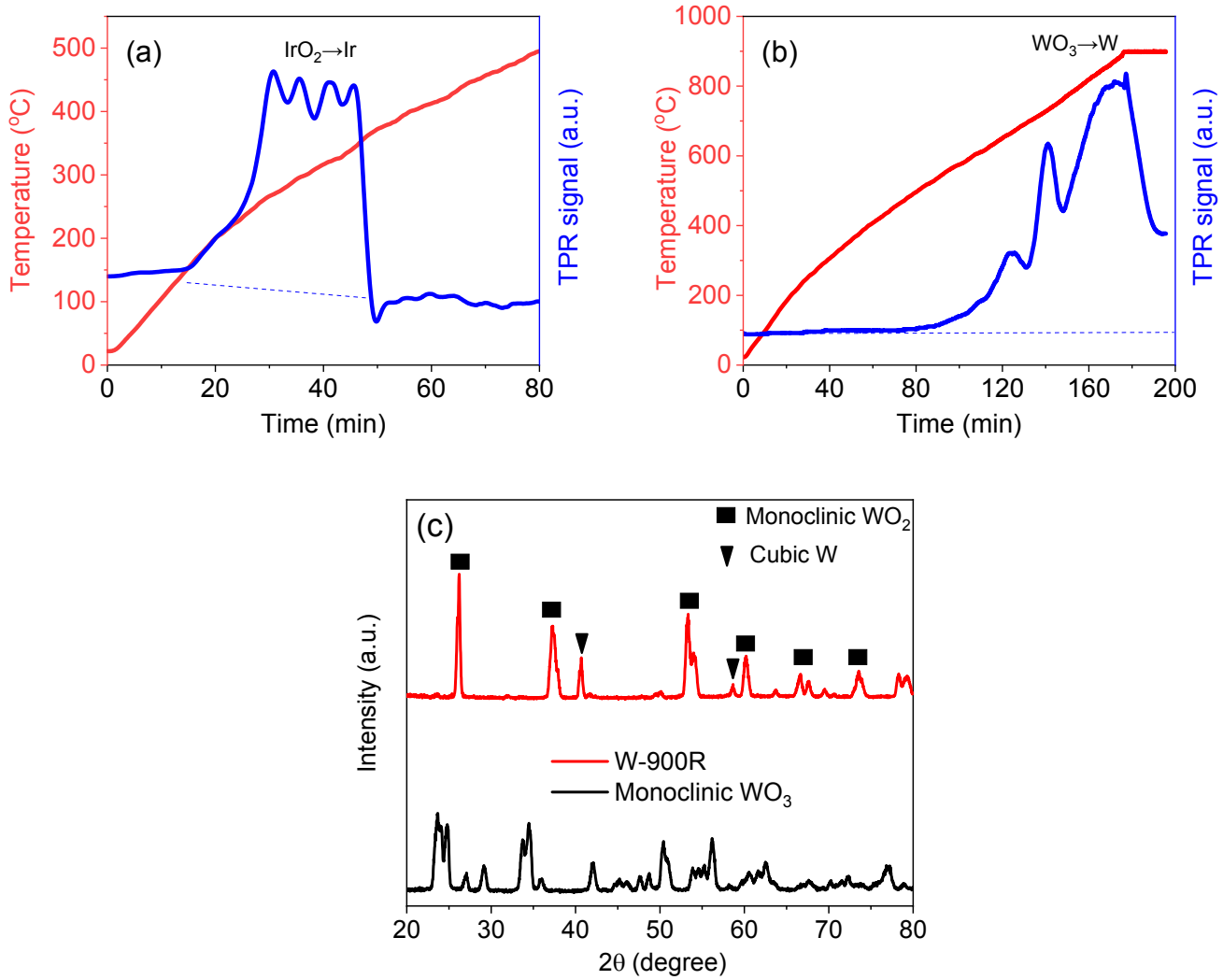

Figure S2. H_2-TPR profiles of IrO_2 (a) and WO_3 (b). Note: It can be seen that the reduction of IrO_2 starts at ~150 °C and ends at ~400 °C, while the reduction of WO_3 starts at 600 °C and can not be completed even at 900 °C for 20 min (because the TPR signal of WO_3 does not return to its original baseline at 900 °C), (c) XRD patterns of WO_3 and W-900R.

Note: From XRD patterns (Figure S2c), it can be seen that W-900R obtained by reducing WO_3 at 900 °C contains metallic W as well as a significant amount of monoclinic WO_2. However, no obvious peaks of WO_2 but only peaks of cubic W are observed in the XRD patterns of $Ir_{0.1}$W-900R and $Ir_{0.5}$W-900R (Figure 2a), suggesting that iridium is able to promote the reduction of tungsten. Moreover, the iridium rich surface can protect the excessive oxidation of tunsten in $Ir_{0.1}$W-900R and $Ir_{0.5}$W-900R after exposure to water for passivation.

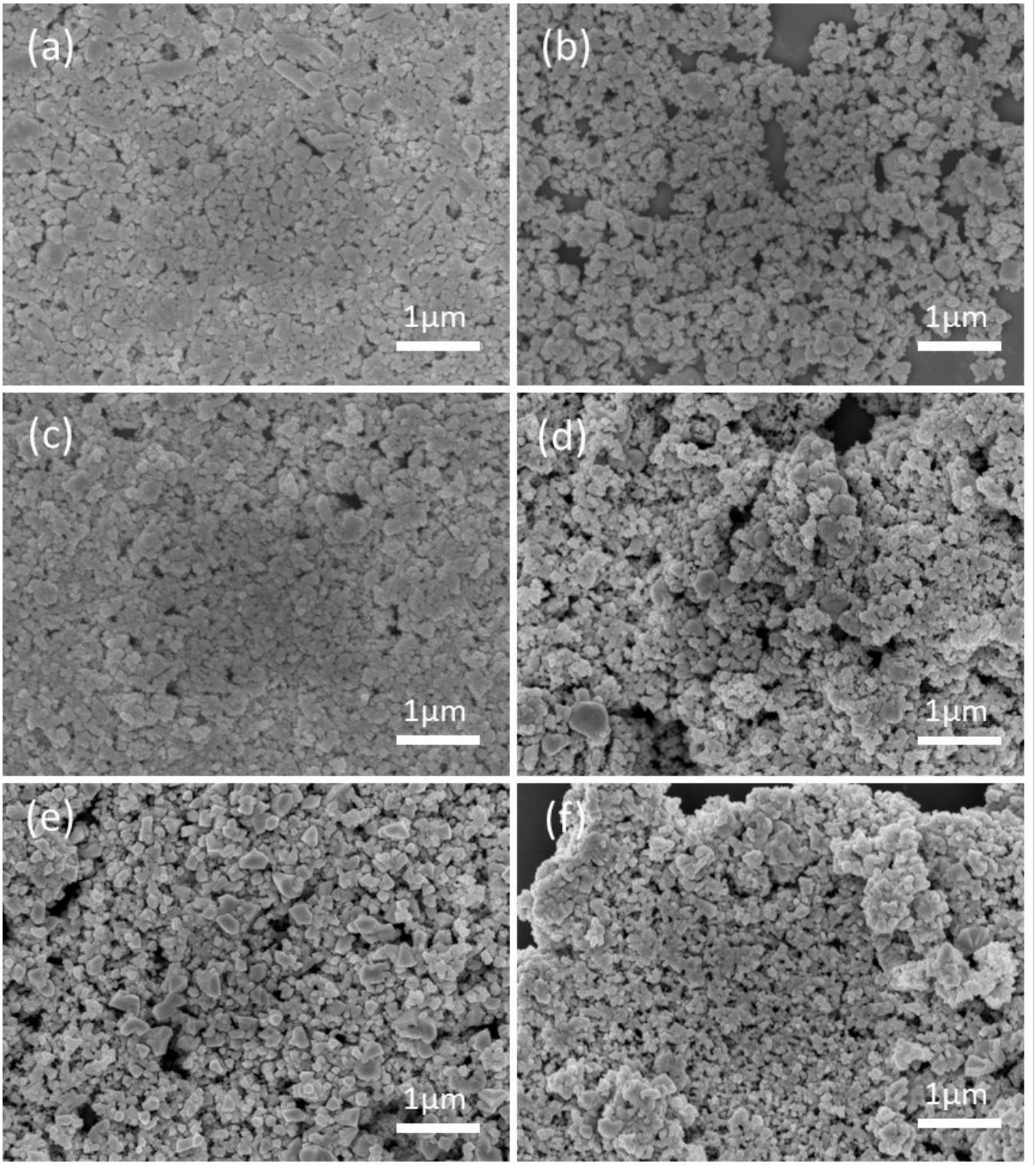

Figure S3. SEM images of (a) $Ir_{0.1}WO_x$, (b) $Ir_{0.1}$W-900R, (c) $Ir_{0.5}WO_x$, (d) $Ir_{0.5}$W-900R, (e) IrO_2, and (f) Ir.

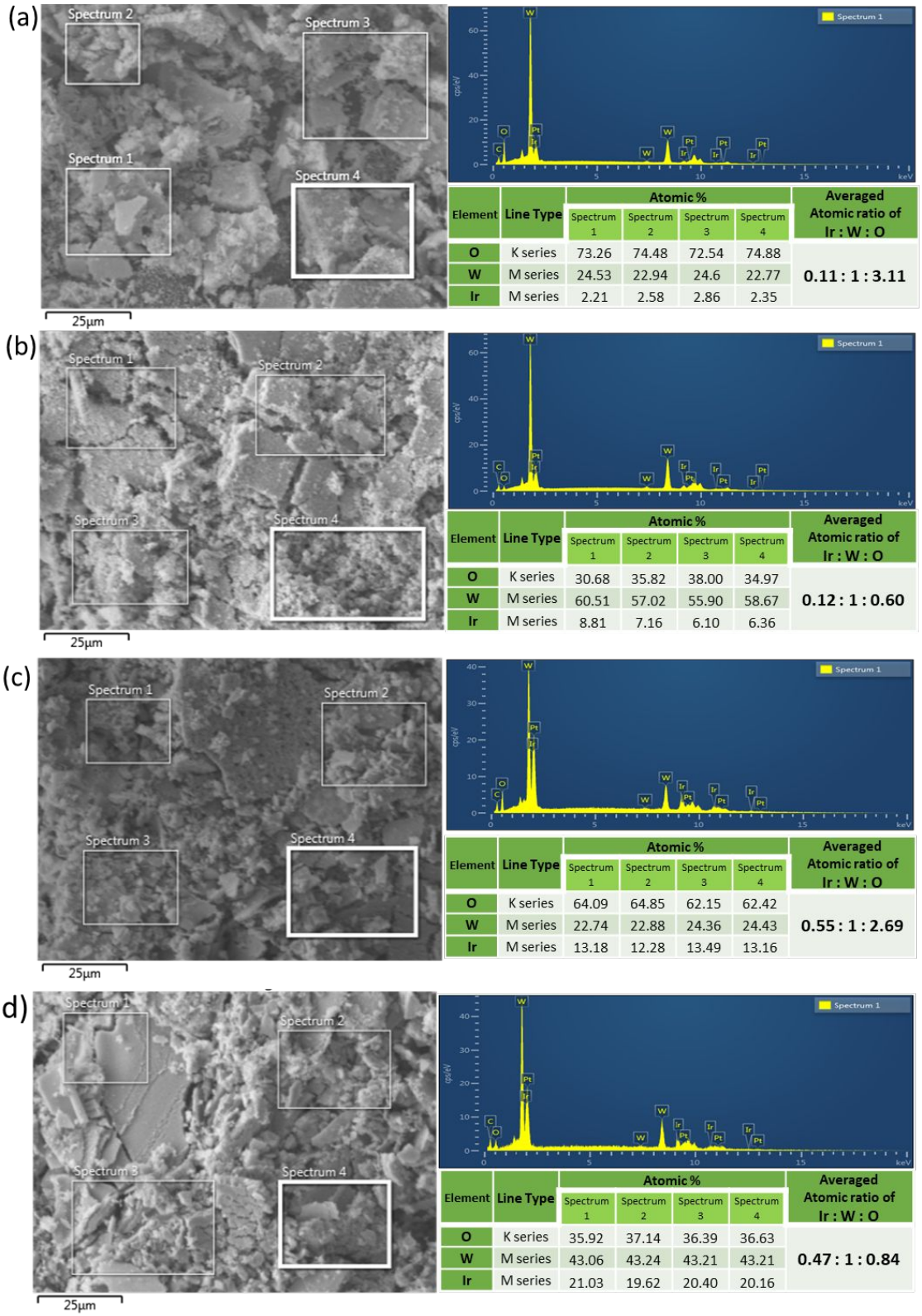

Figure S4. SEM-EDX images of (a) $Ir_{0.1}WO_x$, (b) $Ir_{0.1}$W-900R, (c) $Ir_{0.5}WO_x$, and (d) $Ir_{0.5}$W-900R. Note: Four areas of each sample were selected for EDX spectra collection and one representitive spectrum is given on right. The Pt signal is resulted from the Pt coating prior to SEM measurement. The average atomic ratio of Ir, W, and O elements for each sample are calculated from the atomic compositions obtained in the four spectra.

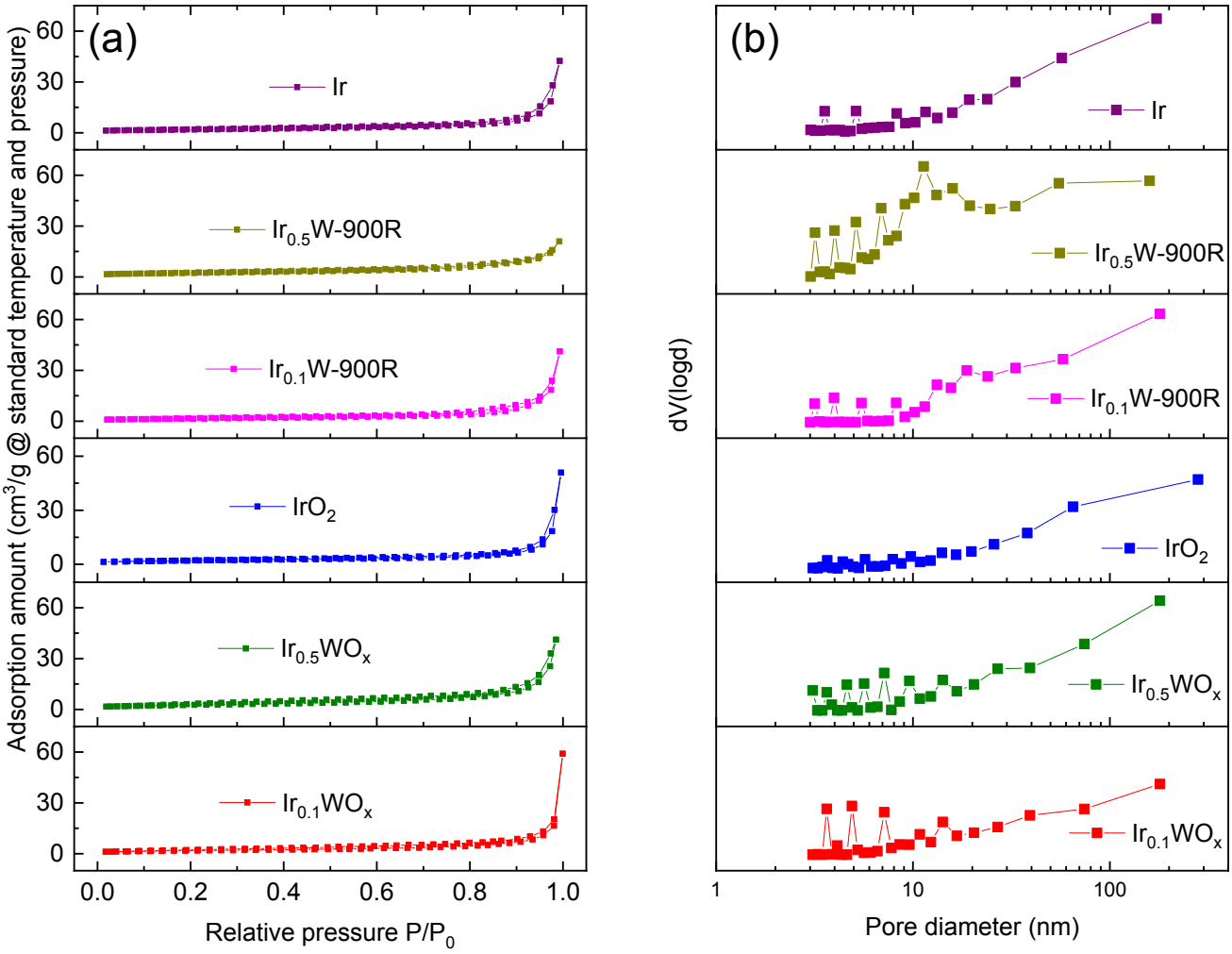

Figure S5. (a) N_2 adsorption-desorption isotherms and (b) BJH pore size distribution of the six samples.

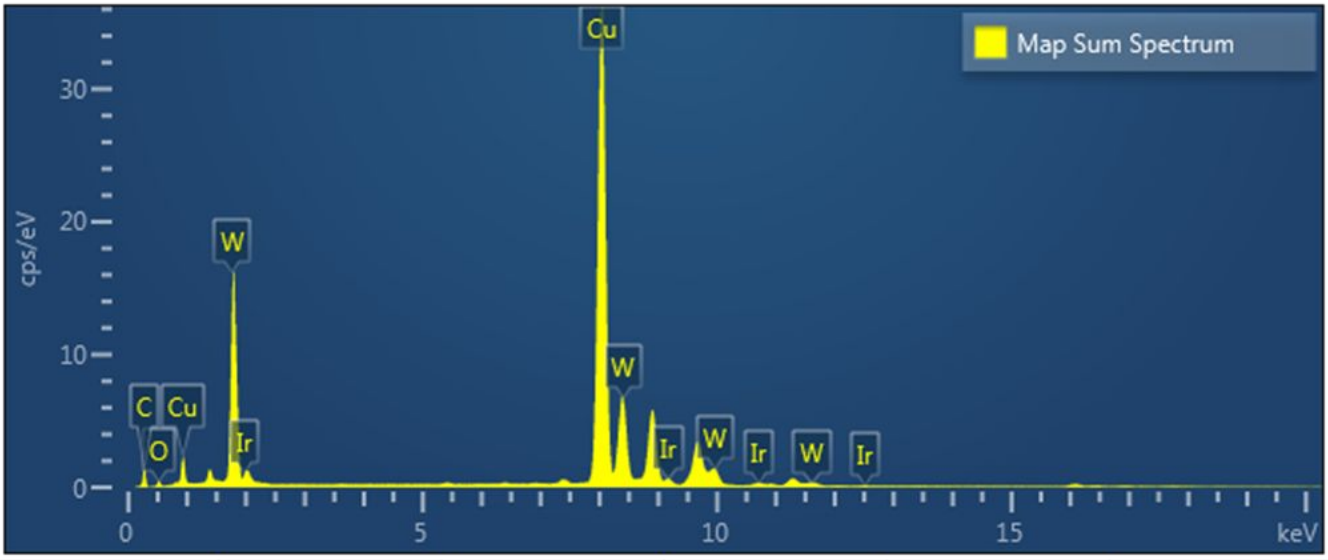

Element	Line Type	k factor	Absorption Correction	Wt%	Wt% Sigma
O	K series	1.86867	1.00	0.78	0.04
W	L series	2.47844	1.00	92.66	0.23
Ir	L series	2.61701	1.00	6.56	0.23
Total:				100.00	

Figure S6. EDX spectrum of $Ir_{0.1}W$-900R and the corresponding elemental composition. The estimated molar ratio of Ir : W is 0.07 : 1 as calculated from the table, generally agrees with the value in Figure S4b.

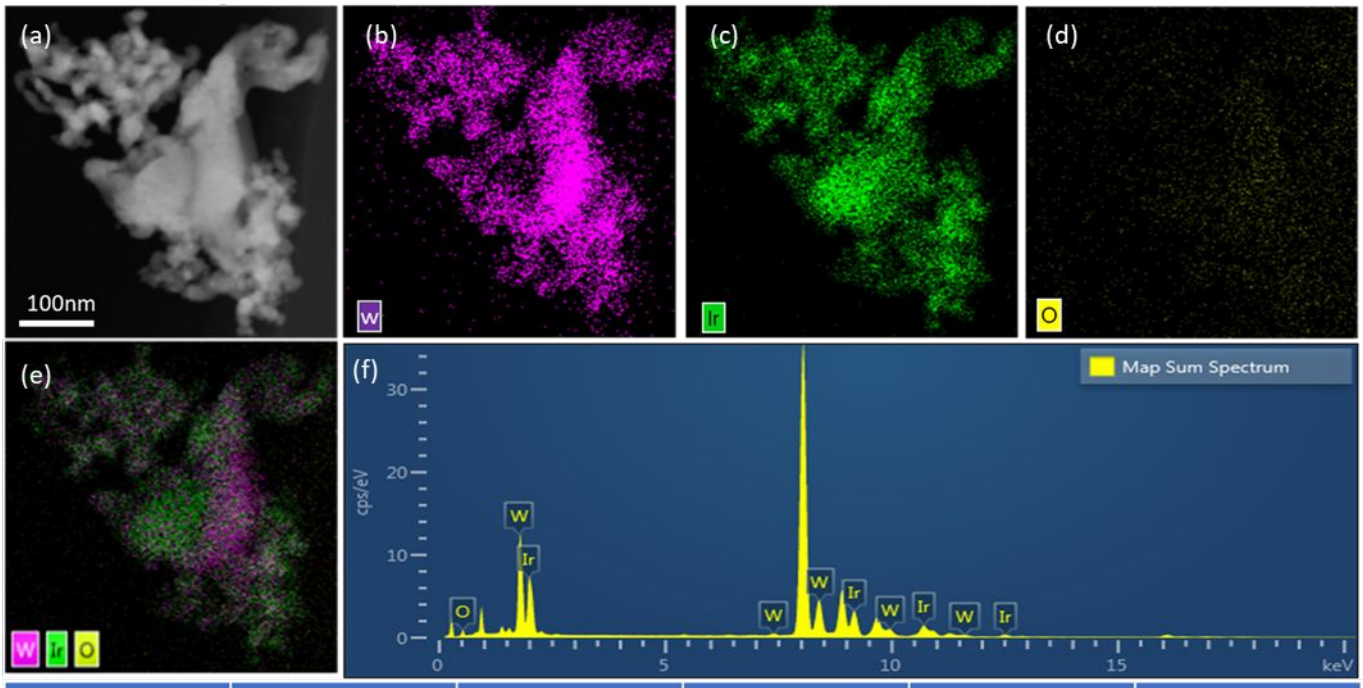

Element	Line Type	k factor	Absorption Correction	Wt%	Wt% Sigma
O	K series	1.86867	1.00	1.17	0.04
W	L series	2.47844	1.00	64.17	0.22
Ir	L series	2.61701	1.00	34.66	0.22
Total:				100.00	

Figure S7. SEM-EDX mapping (a-e) and elemental analysis (f) of $Ir_{0.5}W$-900R. The estimated molar ratio of Ir : W is 0.52 : 1 as calculated from the table, generally agrees with the value in Figure S4d.

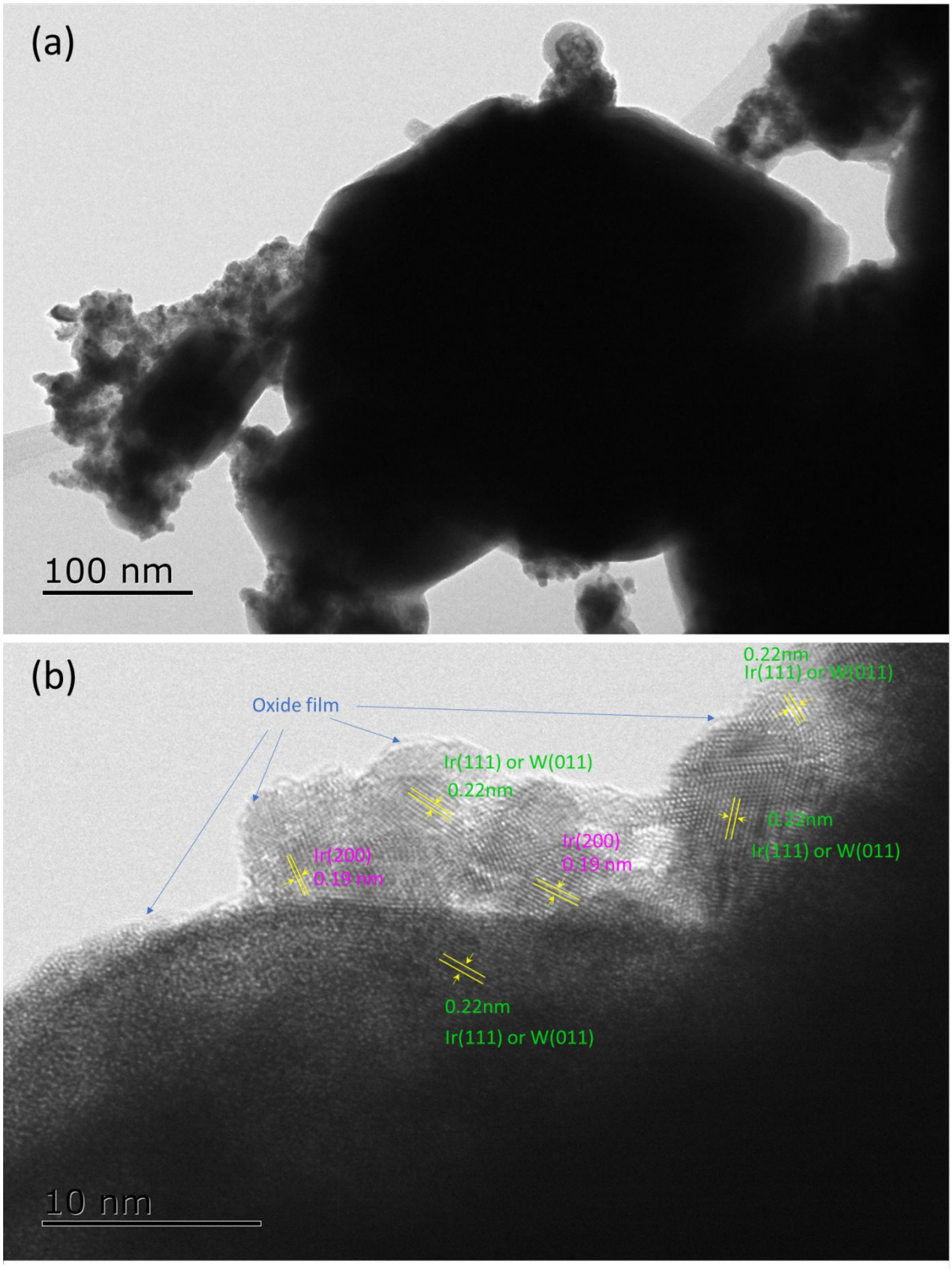

Figure S8. (a-b) Additional TEM images of $Ir_{0.1}W$-900R before CV cycling. Note: lattice spacing of 0.22 nm corresponds to the Ir(111) or W(110) while 0.19 nm corresponds to Ir (200) can be clearly observed.

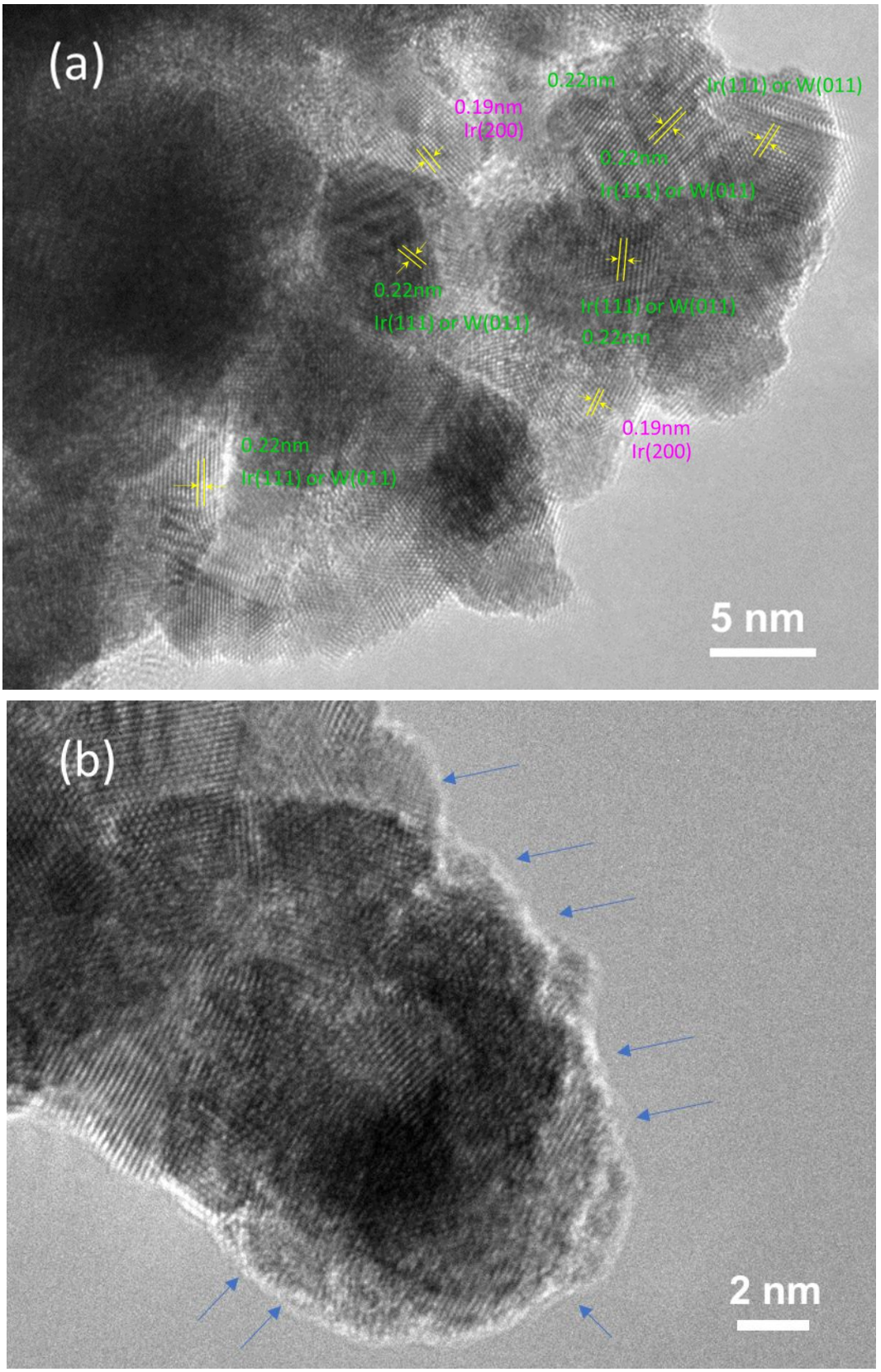

Figure S9. HR-TEM image of $Ir_{0.5}W$-900R before (a) and after (b) the CV activation process. Obvious lattice fringes of metallic W and Ir exist, and the covered oxide film as marked by blue arrows can be observed in less than 1 nm, so the iridium and tungsten should be mixed in sub-nanometer scale.

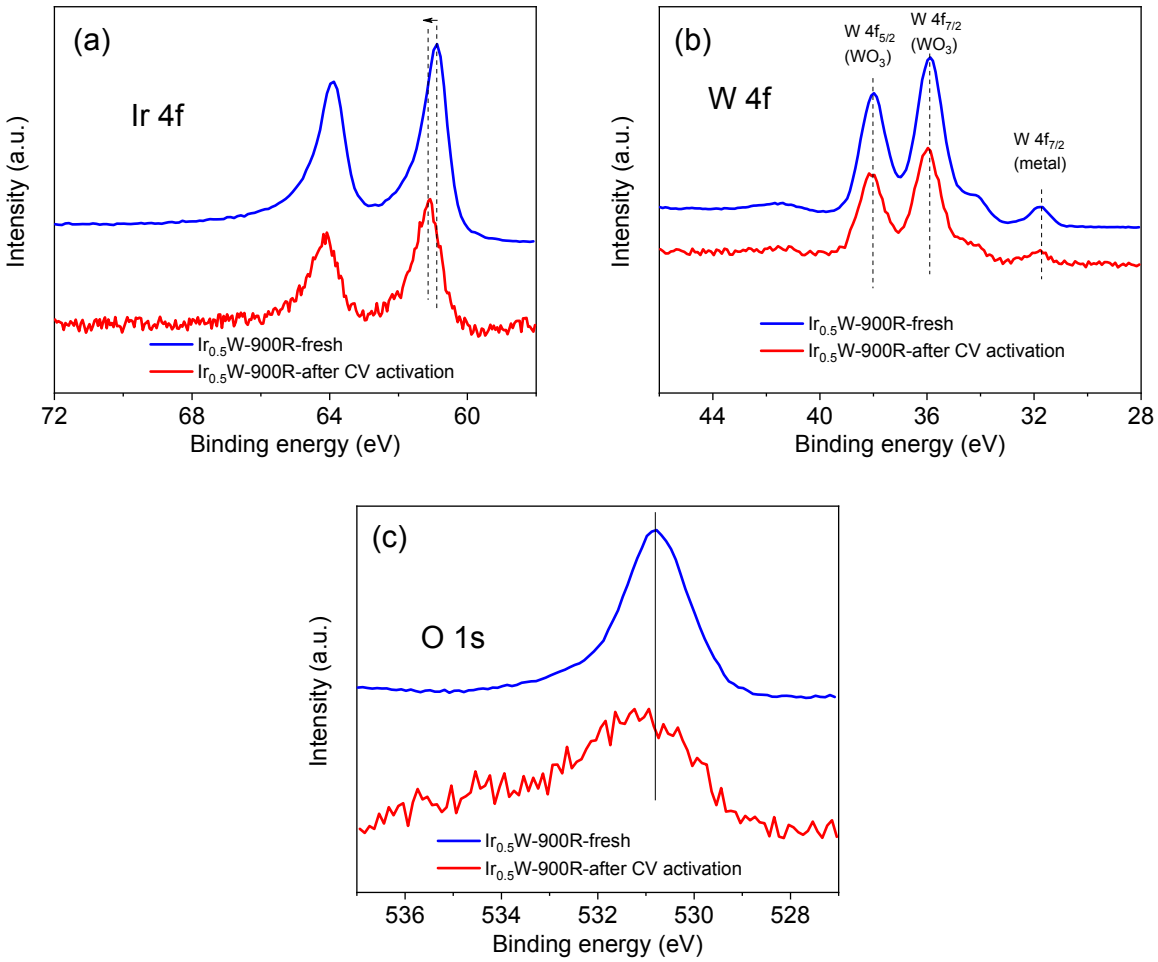

Figure S10. XPS spectra comparation of $Ir_{0.5}W$-900R before and after CV activation: (a) Ir 4f, (b) W 4f, and (c) O 1s.

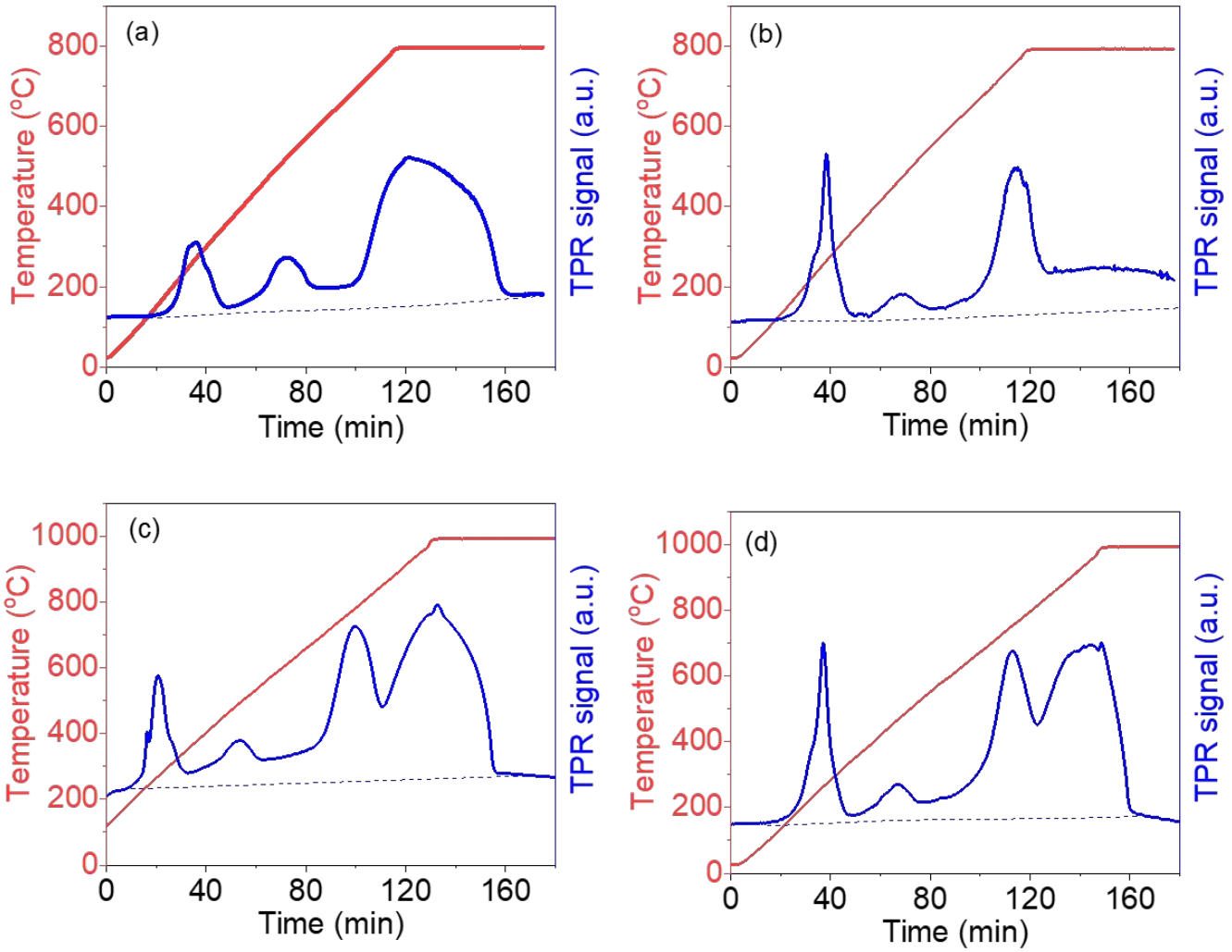

Figure S11. H_2-TPR profiles of $Ir_{0.1}WO_x$ (a and c) and $Ir_{0.5}WO_x$ (b and d). Note: here the slightly different shape of cures compared with Figure 2b and 2c comes from the much less sample amount used in the H_2-TPR process.

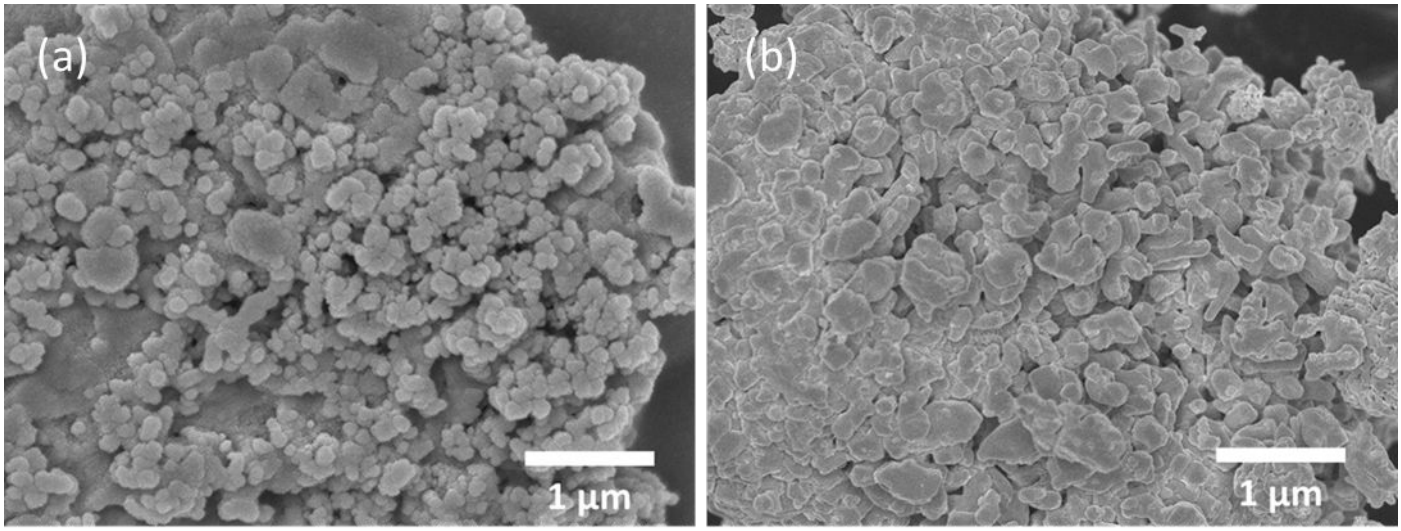

Figure S12. SEM images of $Ir_{0.1}W$-1000R (a) and $Ir_{0.5}W$-1000R (b).

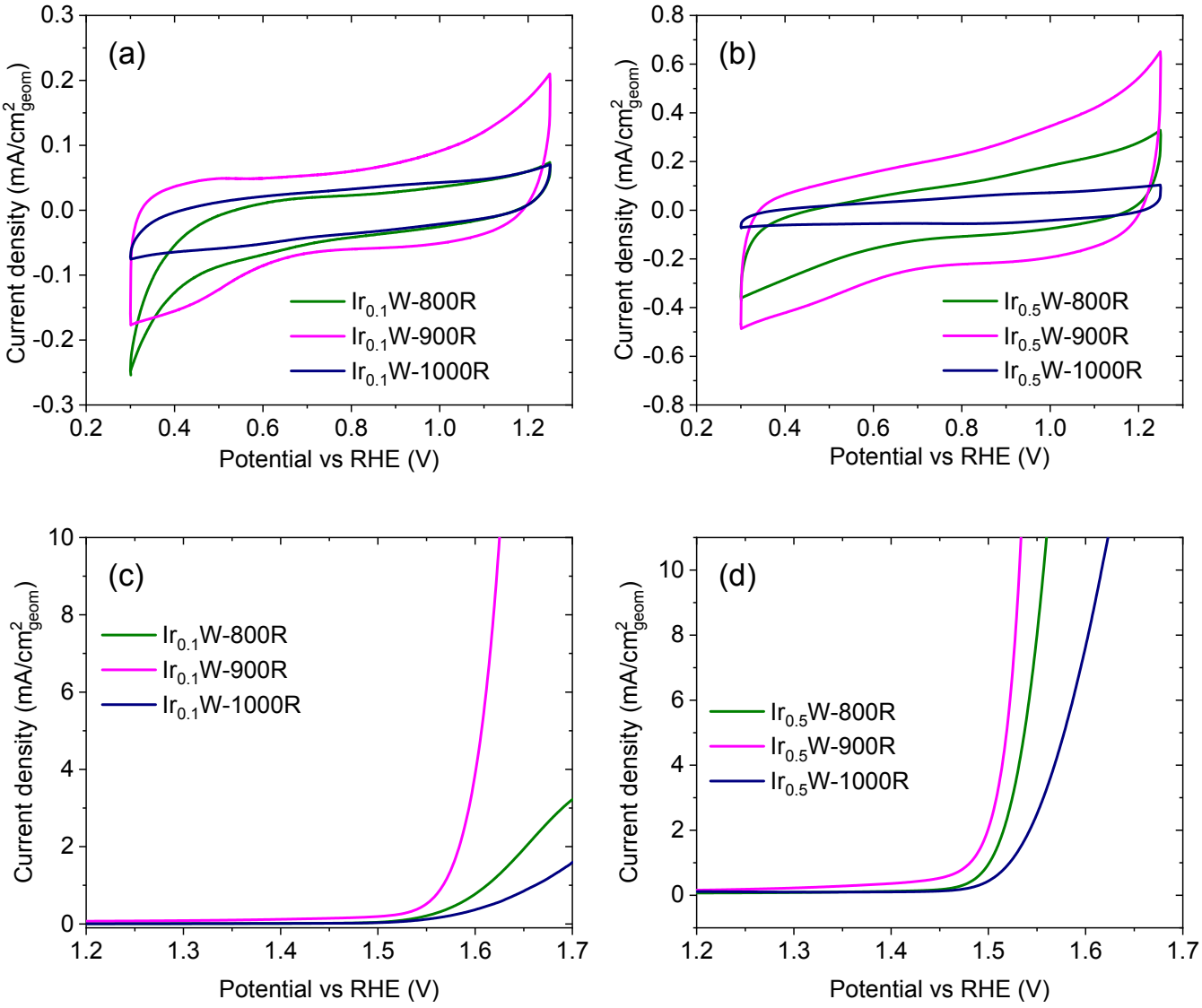

Figure S13. Effect of reduction temperature on the activity of $Ir_{0.1}WO_x$ and $Ir_{0.5}WO_x$: (a and b) CV curves of the reduced catalysts recorded at a scan rate of 50 mV/s and (c and d) LSV curves of the reduced catalysts recorded at a scan rate of 5 mV/s.

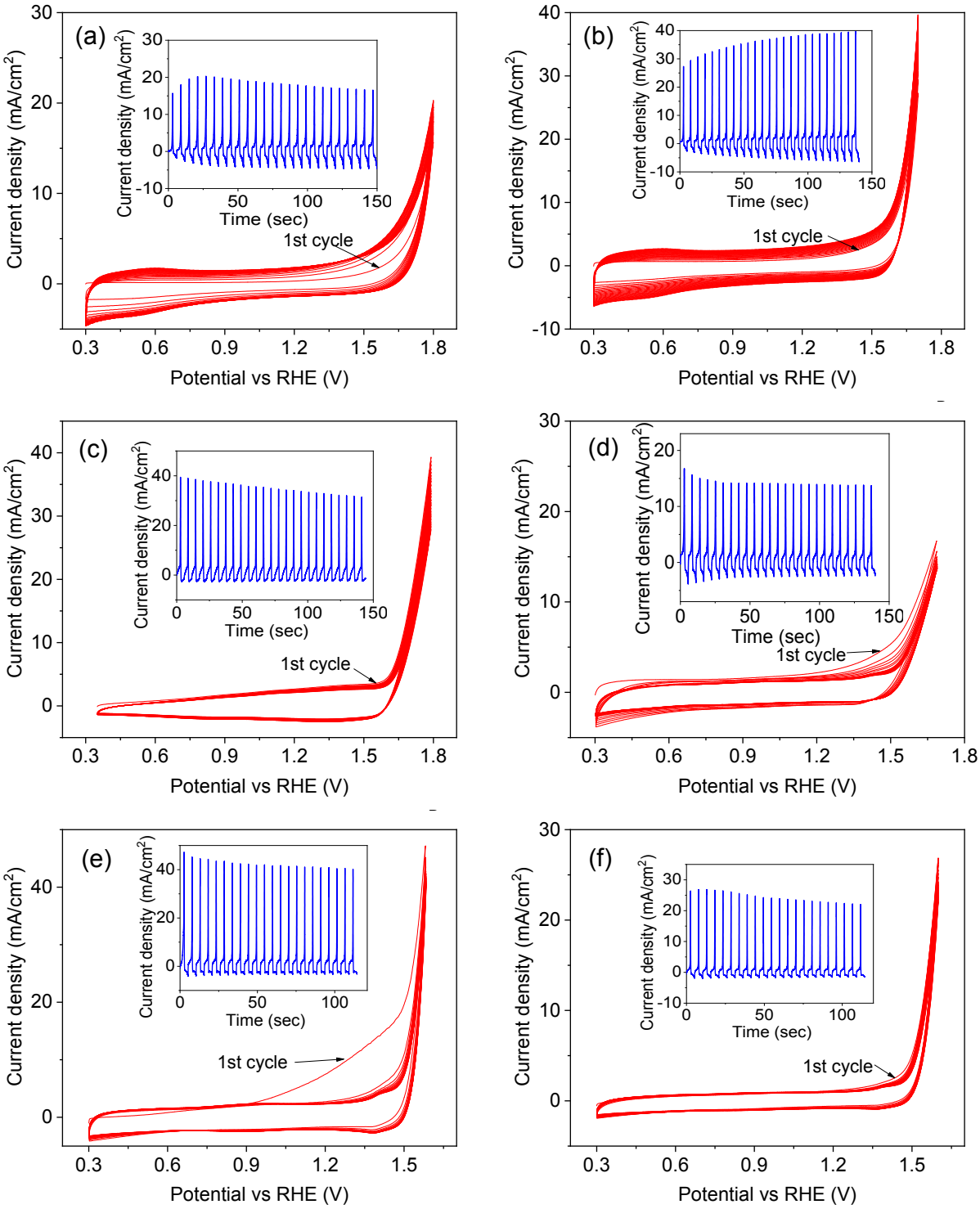

Figure S14. Cyclic voltammetry (CV) curves of the activation process at a scan rate of 500 mV/s and rotating speed of 1600 rpm. Inset shows the current-time plot, suggesting that the catalysts have reached relatively stable activity after 15-25 CV cycles. (a) $Ir_{0.1}WO_x$, (b) $Ir_{0.5}WO_x$, (c) IrO_2, (d) $Ir_{0.1}W$-900R, (e) $Ir_{0.5}W$-900R, and (f) Ir.

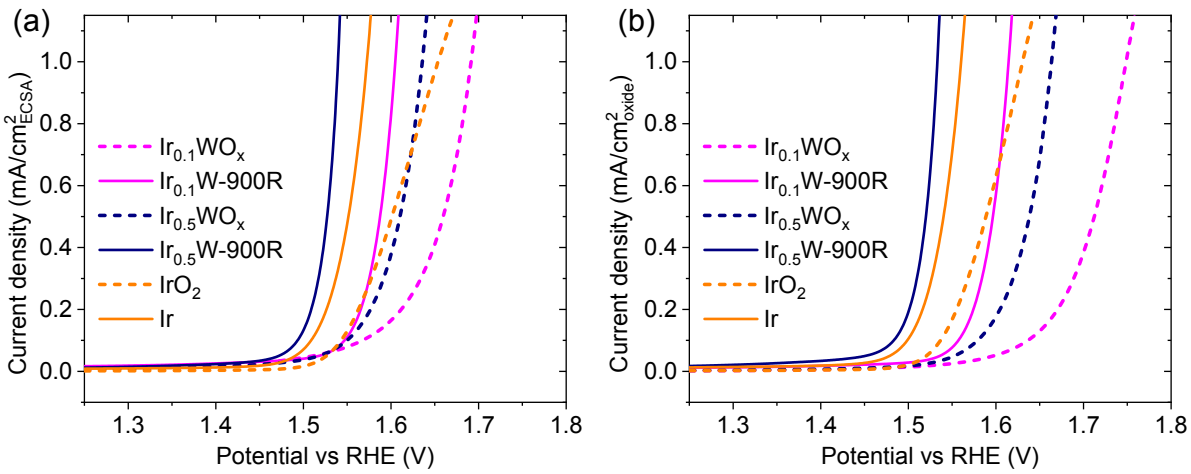

Figure S15. ECSA (a) and specific surface area (b) normalized current density vs. potential of the six catalysts.

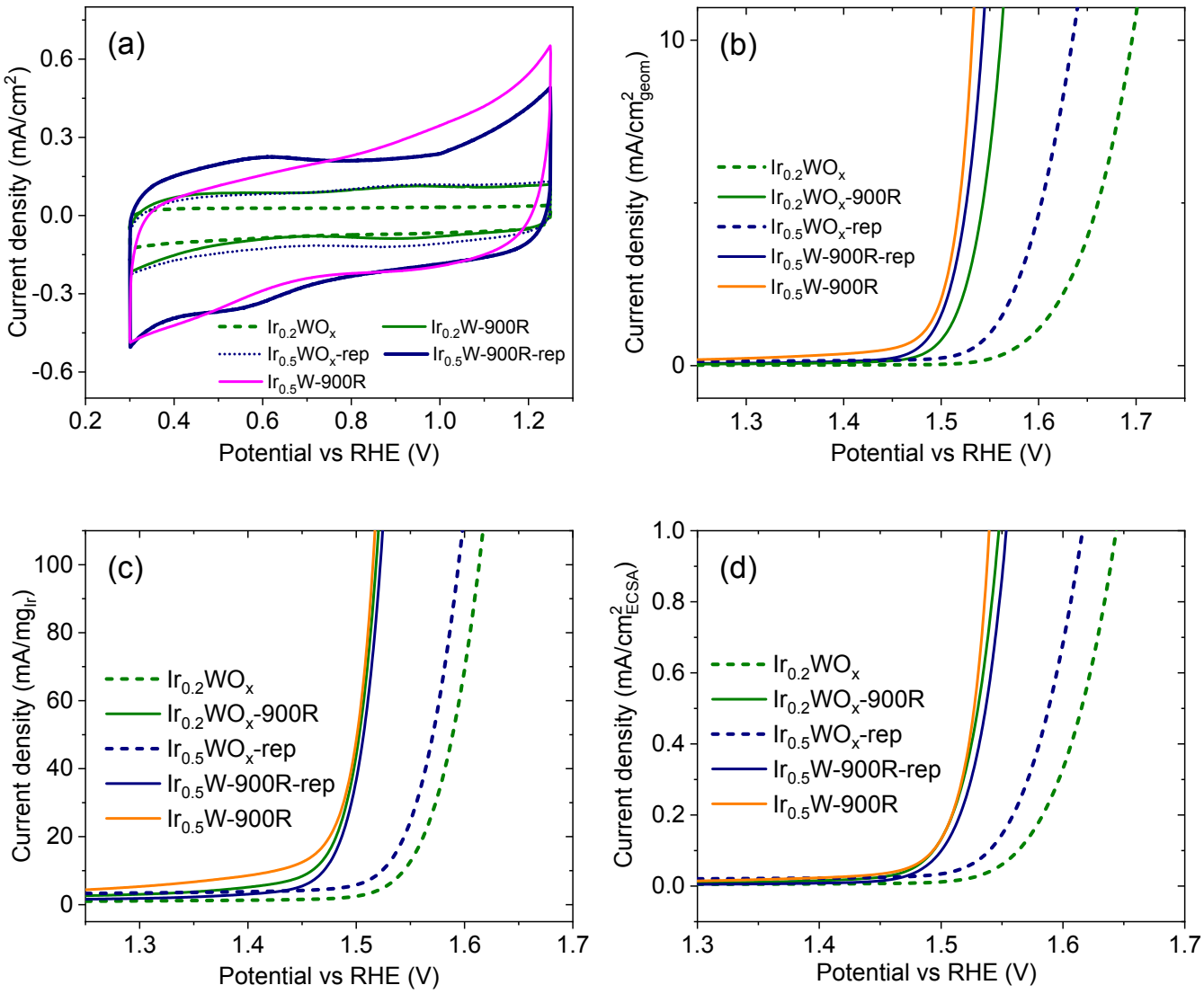

Figure S16. The CV curves (a), geometric area (b), iridium mass (c), and ECSA (d) normalized activity of $Ir_{0.2}WO_x$, $Ir_{0.2}$W-900R, $Ir_{0.5}WO_x$-rep, and $Ir_{0.5}$W-900R-rep. The data of $Ir_{0.5}$W-900R is also added as reference.

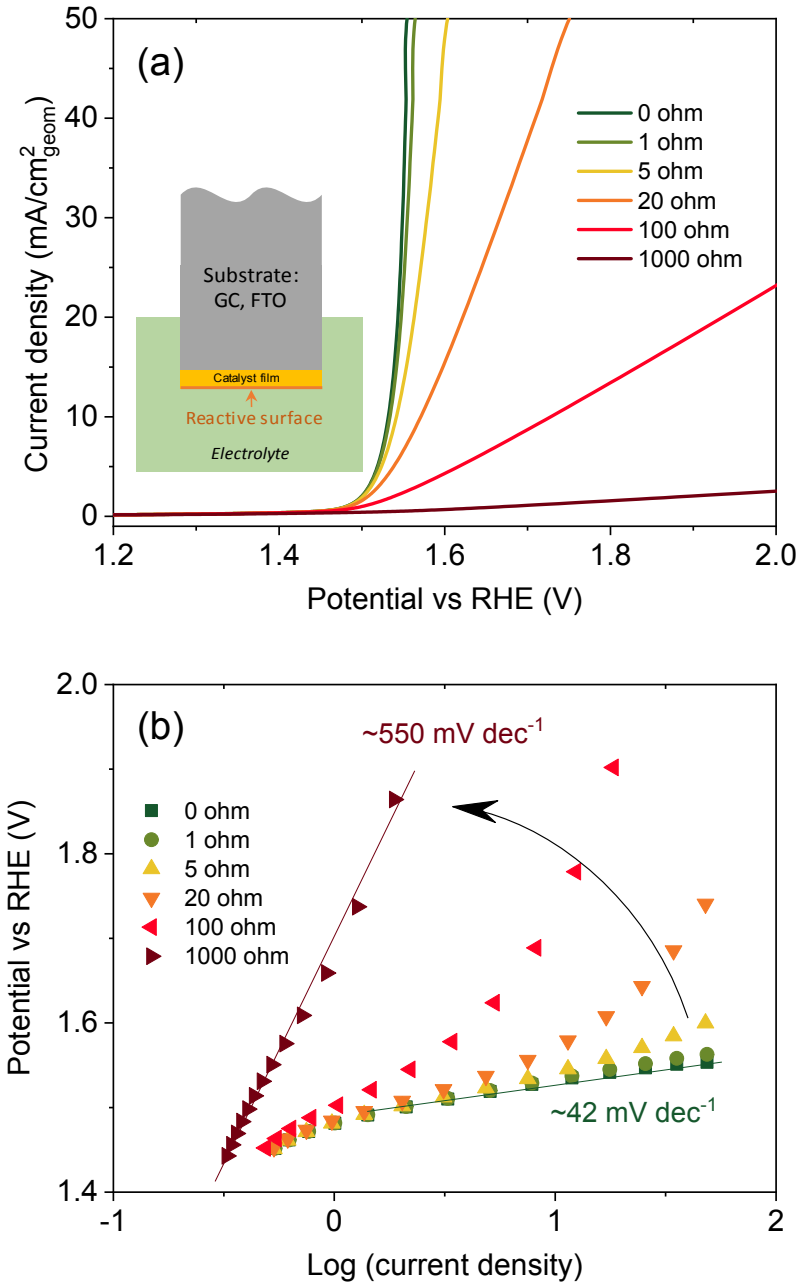

Figure S17. An example showing how the electrical conductivity of the catalyst film affects the apparent activity of the catalyst. The surface reactivity of the catalyst is assumed constant for fair comparison while the resistor of the catalyst film between electrolyte and substrate is increased from 0 Ohm to 1000 Ohm: (a) LSV curves of the catalysts with different film resistance. LSV curve with 0 Ohm resistance is the data of $Ir_{0.5}W$-900R. Inset shows the sketch of the typcial test environment. (b) Tafel slopes of the catalysts with different film resistance derived from LSV curves. It can be seen that the apparent activity decreases together with Tafel slope increasing along with decreasing conductivity of the catalyst, especially at large current range, thus making a good catalyst with high surface reactivity to a poor catalyst, indicating the important role of electrical conductivity on the catalytic performance.

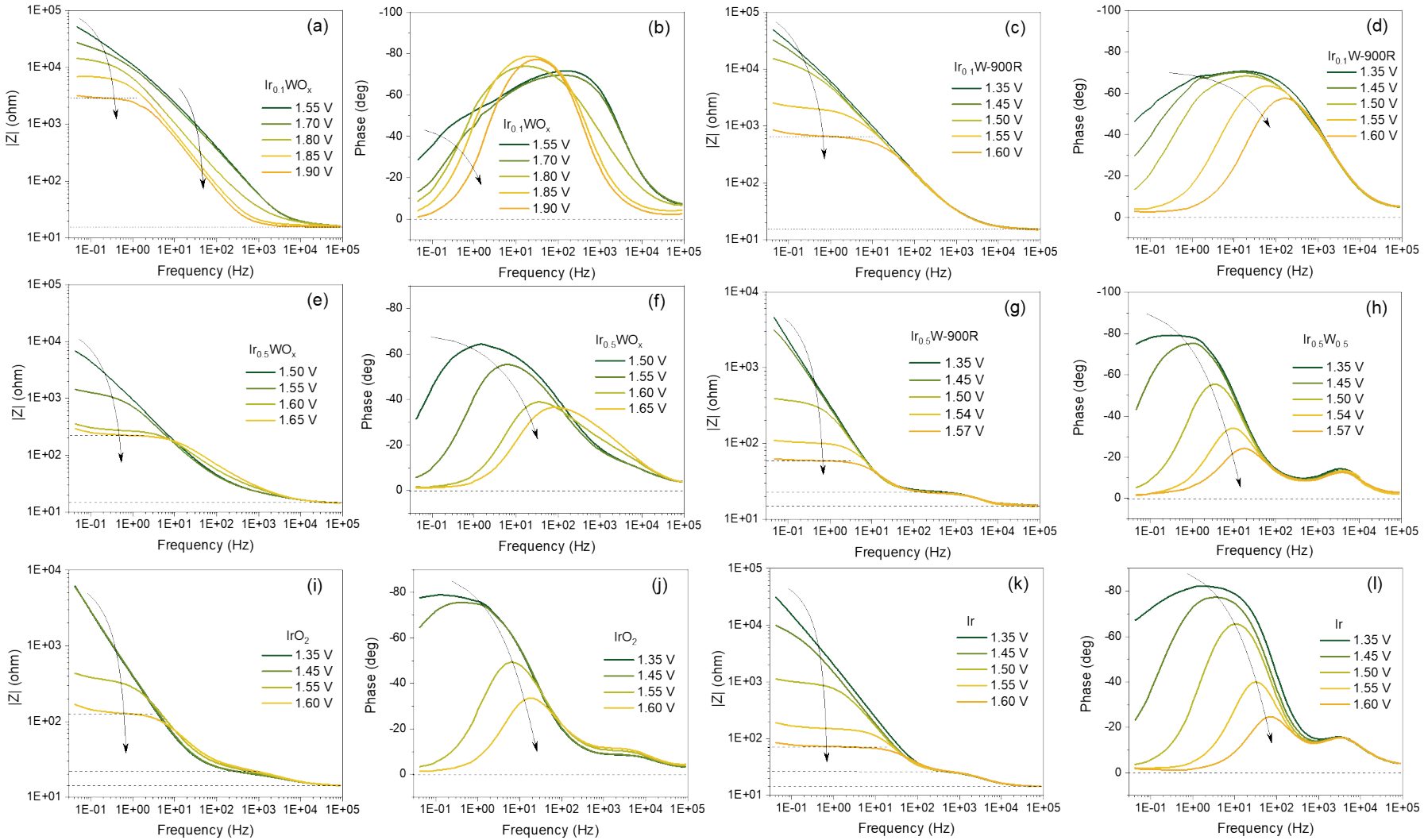

Figure S18. Bode plot of AC impedance over $Ir_{0.1}WO_x$ (a and b), $Ir_{0.1}$W-900R (c and d), $Ir_{0.5}WO_x$ (e and f), $Ir_{0.5}$W-900R (g and h), IrO_2 (i and j), and Ir (k and l) at various potentials.

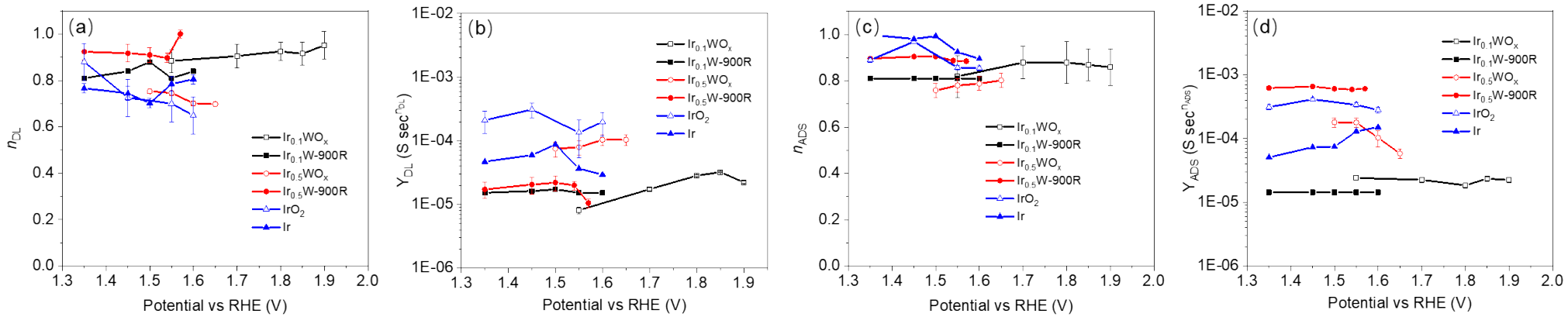

Figure S19. parameters n_{DL} and Y_{01} of constant phase element (Q_{DL}) for double layer capacitor (a & b), and parameters n_2 and Y_{02} of constant phase element (Q_{ADS}) for adsorption pseudocapacitance (c & d).

Note: Impedance over $Ir_{0.1}WO_x$, $Ir_{0.1}$W-900R, and $Ir_{0.5}WO_x$ at low potentials show typical spectra in the ‘‘double-layer” region. The time constants related to the relaxation of the double layer and the coverage of the OER intermediates are similar and difficult to be distinguished even at high potentials, which can be observed in the simulation results as shown in Figure S19. In contrast, two obvious phase change peaks are observable over $Ir_{0.5}$W-900R, IrO_2 and Ir due to the increased adsorption pseudocapacitance at high potentials.

Note: In the equivalent circuit (Figure 6a), constant phase element (CPE) was applied to simulate the imperfect-capacitor behavior of the double layer (Q_{DL}) and intermediates adsorption (Q_{ADS}). The electrical impedance of CPE can be defined as $Z_{CPE} = (j\omega)^{-n}/Y$, where Y and n ($0 < n < 1$) are frequency independent. The constant phase is always $-(90 \times n)°$, with n from 0 to 1. The case of $n = 1$ describes an ideal capacitor while the case of $n = 0$ describes a pure resistor. As the simulation results show that n_{DL} for Q_{DL} and n_{ADS} for Q_{ADS} are close to 1 (Figure S19 a & c) during the measured potential range, Y_{DL} and Y_{ADS} can be roughly considered as the double layer capacitor and adsorption pseudo capacitor for qualitative comparison.[27]

Relaxation time constant for electron transport with charged surface intermediates and reaction rate constant for oxygen evolving catalysis on the surface of nanoparticles are calculated according to a proposed model.[28]

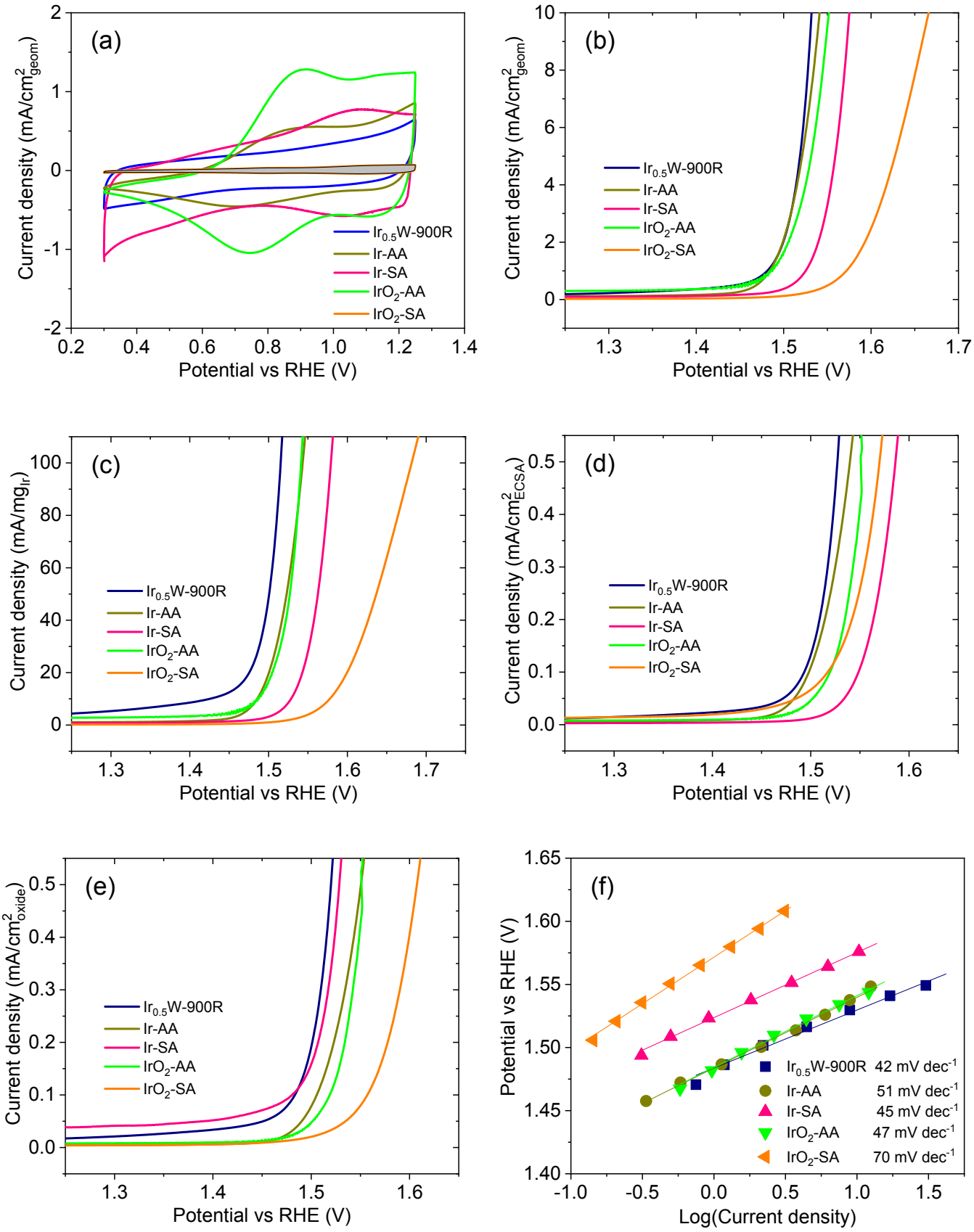

Figure S20. Catalytic activity comparison of $Ir_{0.5}W$-900R with commercial iridium black and iridium oxide. (a) CV curves of the five catalysts, (b-e) LSV curves of geometric area (b), iridium mass (c), ECSA (d), and BET surface area (e) normalized current vs. potential, and (f) Tafel plots of the five catalysts.

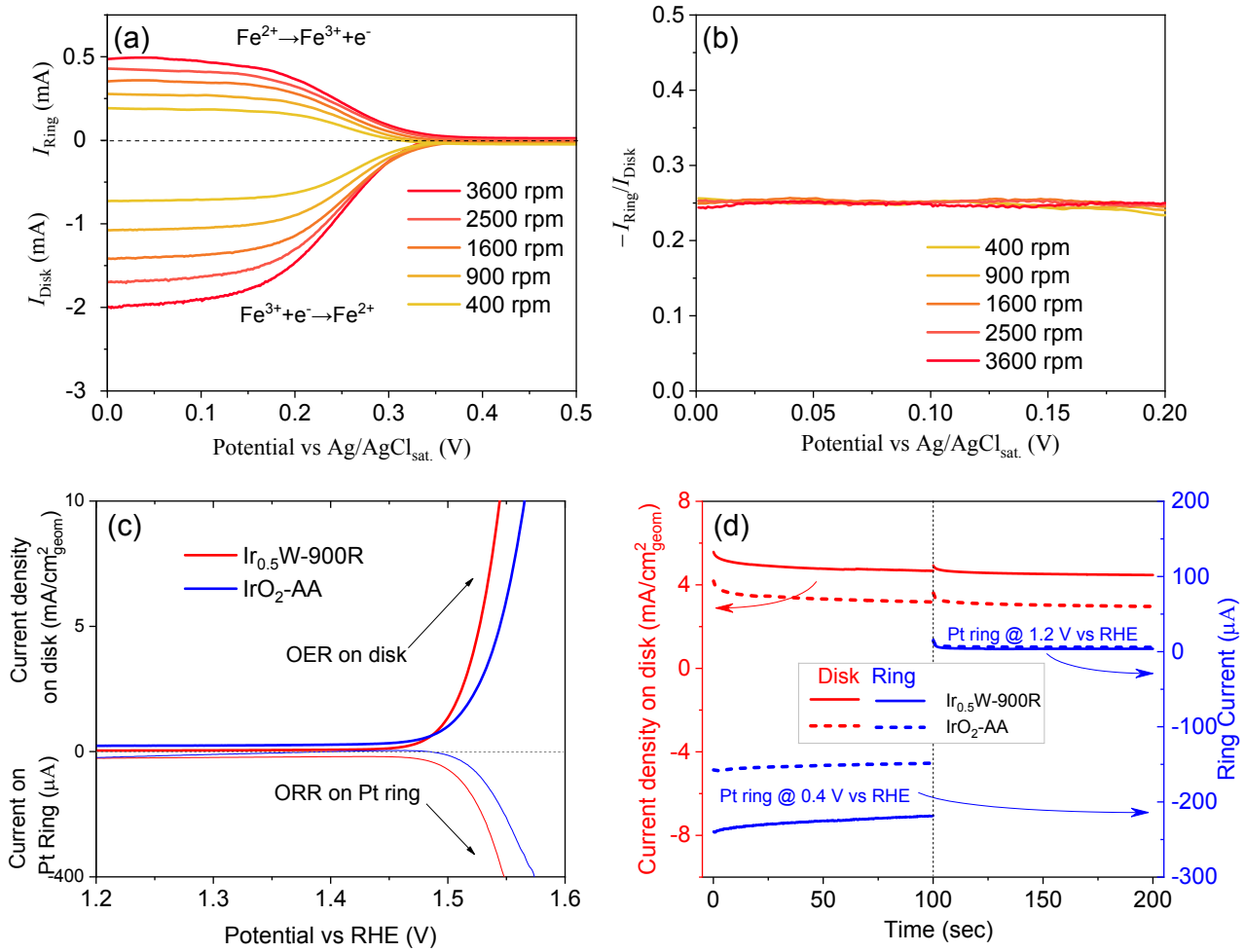

Figure S21. (a & b) Calibration of the collection efficiency of the RRDE by the redox of potassium ferricyanide. (c) LSV curves of commercial IrO_2-AA and $Ir_{0.5}W$-900R using RRDE at 1600 rpm in 0.1 M $HClO_4$; the potential of Pt ring was set at 0.4 V vs. RHE to reduce the oxygen gas generated from catalyst on the disk. (d) Estimation of the faraday efficiency of OER on $Ir_{0.5}W$-900R. Commercial IrO_2-AA was also added as a reference.

Note: An electrolyte containing 10 mM potassium ferricyanide ($K_3Fe(CN)_6$) and 1 M KCl was prepared by dissolving 1 mmol $K_3Fe(CN)_6$ and 0.1 mol KCl in 100 mL ultra-pure water and deoxygenated by bubbling N_2. The redox of $K_3Fe(CN)_6$ was evaluated in a three-electrode configuration with Pt plate as the counter electrode and Ag/AgCl electrode with saturated KCl salt bridge as the reference electrode on a rotating ring disk electrode (RRDE) setup. The potential of the disk was scanned from 0.5 to 0 V vs. Ag/AgCl to reduce Fe^{3+} to Fe^{2+} while the potential of the Pt ring was maintained at 0.5 V vs. Ag/AgCl to oxidize Fe^{2+} to Fe^{3+}. The collection efficiency (CE) of the RRDE was calculated as CE = - I_{Ring}/I_{Disk}, where I_{Ring} is the current on Pt ring and I_{Disk} is the current on glassy carbon disk. The obtained collection efficiency is 0.25, which is consistent with its theoretical value (0.25).

Then, the disk with catalyst was set at a constant potential to conduct OER in 0.1 M $HClO_4$ while the Pt ring was set at 0.4 V vs. RHE to reduce the oxygen gas generated from the disk. It can be seen from Figure S21c that oxygen reduction in Pt ring occurs simultaneously with the OER on both catalysts ($Ir_{0.5}$W-900R and commercial IrO_2-AA). The faraday efficiency of OER on $Ir_{0.5}$W-900R and IrO_2-AA were estimated by the following method[3, 29]: the disk was set at a constant potential to conduct OER while the Pt Ring was set at 0.4 V vs. RHE to reduce the oxygen gas generated from the disk. The current on disk and ring were recorded as shown in Figure S21d. The faraday efficiency was calculated according to:

$$\mathrm{FE} = I_{\mathrm{Ring}}/(I_{\mathrm{disk}} * C_e)$$

C_e is the collection efficiency of the RRDE (0.25).

The calculated faraday efficiency is ~ 96 % for both IrO_2-AA and $Ir_{0.5}$W-900R, the estimated faraday efficiency of IrO_2-AA less than 100 % may be due to the overestimated collection efficiency in oxygen reduction process (The collection efficiency is calibrated by the redox of potassium ferricyanide which is dissolved uniformly in solution. However, the oxygen gas generated from the disk may form some small bubbles, other than dissolved uniformly in solution, thus may affect the collection efficiency of Pt ring.) In addition, the formation of H_2O_2 was excluded by setting the Pt ring at 1.2 V vs. RHE and no obvious oxidation current of H_2O_2 could be detected. In all, it can be concluded that the observed oxidation current on $Ir_{0.5}$W-900R originates from oxygen evolution.

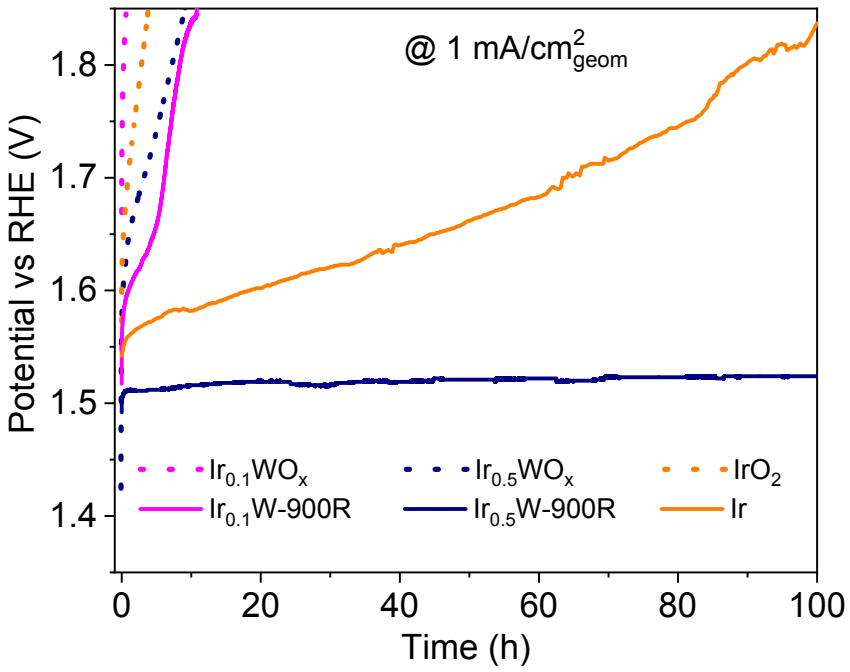

Figure S22. Chronoamperometry test at 1 mA/cm^2 for 100 h.

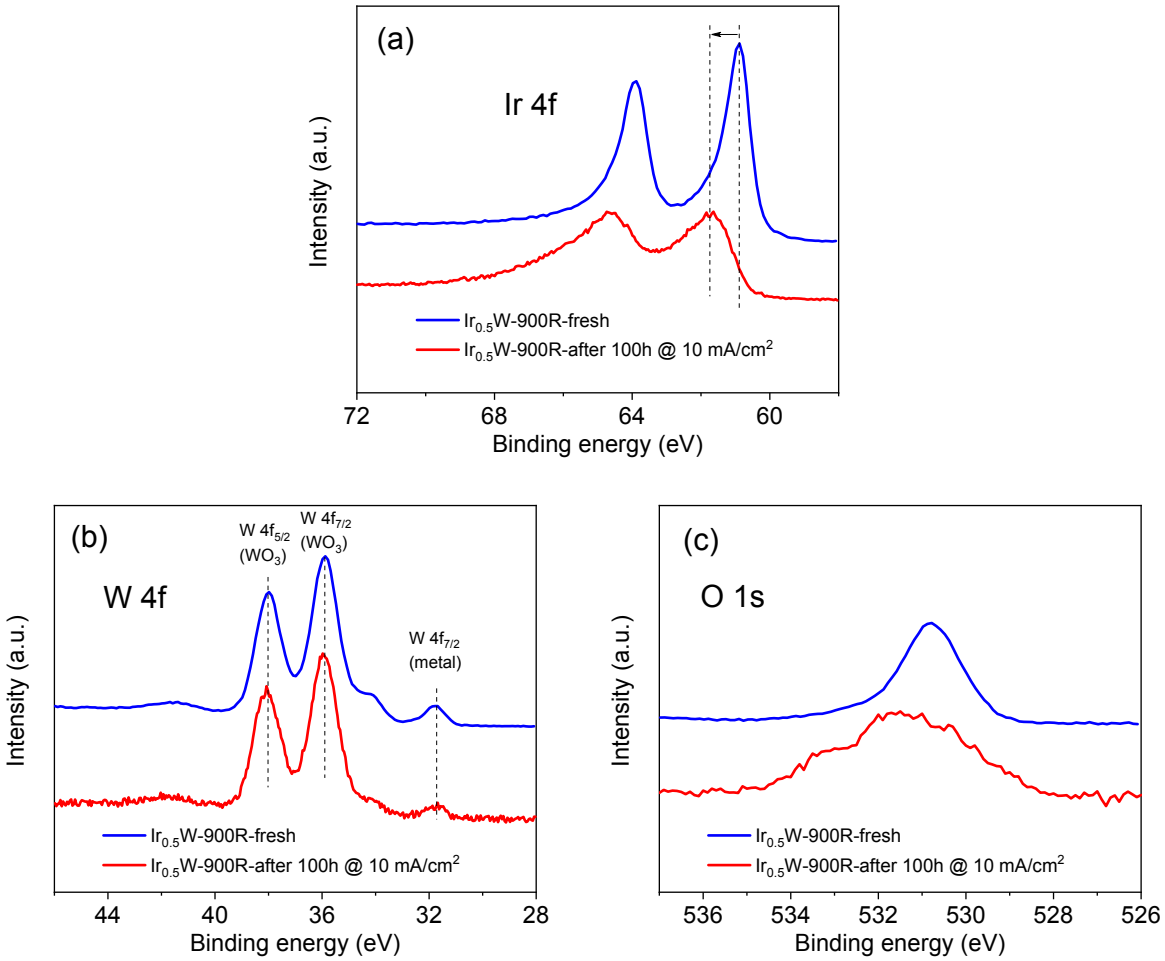

Figure S23. Comparison of the XPS spectra for $Ir_{0.5}W$-900R before and after stability test: (a) Ir 4f, the iridium species on $Ir_{0.5}W$-900R after stability test is mainly in +4 valence state, (b) W 4f, and (c) O 1s.

References

1. Zhao, S.; Yu, H.; Maric, R.; Danilovic, N.; Capuano, C. B.; Ayers, K. E.; Mustain, W. E., Calculating the Electrochemically Active Surface Area of Iridium Oxide in Operating Proton Exchange Membrane Electrolyzers. *J. Electrochem. Soc.* **2015,** *162*, F1292-F1298.

2. Lyons, M. E. G.; Floquet, S., Mechanism of Oxygen Reactions at porous Oxide Electrodes. Part 2-Oxygen Evolution at RuO_2, IrO_2 and $Ir_xRu_{1-x}O_2$ Electrodes in Aqueous Acid and Alkaline Solution. *Phys. Chem. Chem. Phys.* **2011,** *13*, 5314-5335.

3. Suntivich, J.; May, K. J.; Gasteiger, H. A.; Goodenough, J. B.; Shao-Horn, Y., A Perovskite Oxide Optimized for Oxygen Evolution Catalysis from Molecular Orbital Principles. *Science* **2011,** *334*, 1383-1385.

4. Perdew, J. P.; Ernzerhof, M.; Burke, K., Rationale for Mixing Exact Exchange with Density Functional Approximations. *J. Chem. Phys.* **1996,** *105*, 9982-9985.

5. Hammer, B.; Hansen, L. B.; Nørskov, J. K., Improved Adsorption Energetics within Density-Functional Theory using Revised Perdew-Burke-Ernzerhof Functionals. *Phys. Rev. B* **1999,** *59*, 7413-7421.

6. Perdew, J. P.; Burke, K.; Ernzerhof, M., Generalized Gradient Approximation Made Simple. *Phys. Rev. Lett.* **1996,** *77*, 3865-3868.

7. Kresse, G.; Joubert, D., From Ultrasoft Pseudopotentials to the Projector Augmented-Wave Method. *Phys. Rev. B* **1999,** *59*, 1758-1775.

8. Kresse, G.; Furthmüller, J., Efficient Iterative Schemes for Ab Initio Total-Energy Calculations using A Plane-Wave Basis Set. *Phys. Rev. B* **1996,** *54*, 11169-11186.

9. Kresse, G.; Furthmüller, J., Efficiency of ab-initio Total Energy Calculations for Metals and Semiconductors using a Plane-Wave Basis Set. *Comput. Mater. Sci.* **1996,** *6*, 15-50.

10. Deskins, N. A.; Rousseau, R.; Dupuis, M., Defining the Role of Excess Electrons in the Surface Chemistry of TiO_2. *J. Phys. Chem. C* **2010,** *114*, 5891-5897.

11. Yang, J.-t.; Ma, C.; Ge, C.; Zhang, Q.-h.; Du, J.-y.; Li, J.-k.; Huang, H.-y.; He, M.; Wang, C.; Meng, S.;

Gu, L.; Lu, H.-b.; Yang, G.-z.; Jin, K.-j., Effects of Line Defects on The Electronic and Optical Properties of Strain-Engineered WO_3 Thin Films. *J. Mater. Chem. C* **2017,** *5*, 11694-11699.

12. Dudarev, S. L.; Botton, G. A.; Savrasov, S. Y.; Humphreys, C. J.; Sutton, A. P., Electron-Energy-Loss Spectra and the Structural Stability of Nickel Oxide: An LSDA+U study. *Phys. Rev. B* **1998,** *57*, 1505-1509.

13. Man, I. C.; Su, H.-Y.; Calle-Vallejo, F.; Hansen, H. A.; Martínez, J. I.; Inoglu, N. G.; Kitchin, J.; Jaramillo, T. F.; Nørskov, J. K.; Rossmeisl, J., Universality in Oxygen Evolution Electrocatalysis on Oxide Surfaces. *ChemCatChem* **2011,** *3*, 1159-1165.

14. Cramer, C. J., *Essentials of Computational Chemistry: Theories and Models*. 2nd ed.; Wiley: 2004.

15. Nørskov, J. K.; Rossmeisl, J.; Logadottir, A.; Lindqvist, L.; Kitchin, J. R.; Bligaard, T.; Jonsson, H., Origin of the Overpotential for Oxygen Reduction at A Fuel-Cell Cathode. *J. P. Chem. B* **2004,** *108*, 17886-17892.

16. Gao, J.; Xu, C. Q.; Hung, S. F.; Liu, W.; Cai, W.; Zeng, Z.; Jia, C.; Chen, H. M.; Xiao, H.; Li, J.; Huang, Y.; Liu, B., Breaking Long-Range Order in Iridium Oxide by Alkali Ion for Efficient Water Oxidation. *J. Am. Chem. Soc.* **2019,** *141*, 3014-3023.

17. Nong, H. N.; Reier, T.; Oh, H.-S.; Gliech, M.; Paciok, P.; Vu, T. H. T.; Teschner, D.; Heggen, M.; Petkov, V.; Schlögl, R.; Jones, T.; Strasser, P., A Unique Oxygen Ligand Environment Facilitates Water Oxidation in Hole-Doped IrNiOx Core–Shell Electrocatalysts. *Nature Catal.* **2018,** *1*, 841-851.

18. Lee, Y.; Suntivich, J.; May, K. J.; Perry, E. E.; Shao-Horn, Y., Synthesis and Activities Of Rutile IrO_2 and RuO_2 Nanoparticles for Oxygen Evolution in Acid and Alkaline Solutions. *J. Phys. Chem. Lett.* **2012,** *3*, 399-404.

19. McCrory, C. C. L.; Jung, S.; Ferrer, I. M.; Chatman, S. M.; Peters, J. C.; Jaramillo, T. F., Benchmarking Hydrogen Evolving Reaction and Oxygen Evolving Reaction Electrocatalysts for Solar Water Splitting Devices. *J. Am. Chem. Soc.* **2015,** *137*, 4347-4357.

20. Oh, H. S.; Nong, H. N.; Reier, T.; Gliech, M.; Strasser, P., Oxide-Supported Ir Nanodendrites with High Activity and Durability for the Oxygen Evolution Reaction in Acid PEM Water Electrolyzers. *Chem. Sci.* **2015,** *6*, 3321-3328.

21. Diaz-Morales, O.; Raaijman, S.; Kortlever, R.; Kooyman, P. J.; Wezendonk, T.; Gascon, J.; Fu, W. T.; Koper, M. T., Iridium-based Double Perovskites for Efficient Water Oxidation in Acid Media. *Nat. Commun.* **2016,** *7*, 12363.

22. Lebedev, D.; Povia, M.; Waltar, K.; Abdala, P. M.; Castelli, I. E.; Fabbri, E.; Blanco, M. V.; Fedorov, A.; Copéret, C.; Marzari, N.; Schmidt, T. J., Highly Active and Stable Iridium Pyrochlores for Oxygen Evolution Reaction. *Chem. Mater.* **2017,** *29*, 5182-5191.

23. Seitz, L. C.; Dickens, C. F.; Nishio, K.; Hikita, Y.; Montoya, J.; Doyle, A.; Kirk, C.; Vojvodic, A.; Hwang, H. Y.; Norskov, J. K.; Jaramillo, T. F., A Highly Active and Stable $IrO_x/SrIrO_3$ Catalyst for the Oxygen Evolution Reaction. *Science* **2016,** *353*, 1011-1014.

24. Massue, C.; Pfeifer, V.; Huang, X.; Noack, J.; Tarasov, A.; Cap, S.; Schlogl, R., High-performance Supported Iridium Oxohydroxide Water Oxidation Electrocatalysts. *ChemSusChem* **2017,** *10*, 1943-1957.

25. Abbott, D. F.; Lebedev, D.; Waltar, K.; Povia, M.; Nachtegaal, M.; Fabbri, E.; Coperet, C.; Schmidt, T. J., Iridium Oxide for the Oxygen Evolution Reaction: Correlation between Particle Size, Morphology, and the Surface Hydroxo Layer from Operando XAS. *Chem. Mater.* **2016,** *28*, 6591-6604.

26. Reier, T.; Pawolek, Z.; Cherevko, S.; Bruns, M.; Jones, T.; Teschner, D.; Selve, S.; Bergmann, A.; Nong, H. N.; Schlogl, R.; Mayrhofer, K. J.; Strasser, P., Molecular Insight in Structure and Activity of Highly Efficient, Low-Ir Ir-Ni Oxide Catalysts for Electrochemical Water Splitting (OER). *J. Am. Chem. Soc.* **2015,** *137*, 13031-13040.

27. Hsu, C. H.; Mansfeld, F., Concerning the Conversion of the Constant Phase Element Parameter Y_0 into a Capacitance. *Corrosion* **2001,** *57*, 747-748.

28. Seo, H.; Jin, K.; Park, S.; Cho, K. H.; Ha, H.; Lee, K.-G.; Lee, Y. H.; Nguyen, D. T.; Randriamahazaka, H.; Lee, J.-S.; Nam, K. T., Mechanistic Investigation with Kinetic Parameters on Water Oxidation Catalyzed by Manganese Oxide Nanoparticle Film. *ACS Sustainable Chem. Eng.* **2019,** *7*, 10595-10604.

29. Yao, Y.; Hu, S.; Chen, W.; Huang, Z.-Q.; Wei, W.; Yao, T.; Liu, R.; Zang, K.; Wang, X.; Wu, G.; Yuan, W.; Yuan, T.; Zhu, B.; Liu, W.; Li, Z.; He, D.; Xue, Z.; Wang, Y.; Zheng, X.; Dong, J.; Chang, C.-R.; Chen, Y.; Hong, X.; Luo, J.; Wei, S.; Li, W.-X.; Strasser, P.; Wu, Y.; Li, Y., Engineering the Electronic Structure of Single Atom Ru Sites via Compressive Strain Boosts Acidic Water Oxidation Electrocatalysis. *Nature Catal.* **2019,** *2*, 304-313.